Surface & Coatings Technology 458 (2023) 129343

Contents lists available at ScienceDirect

Surface & Coatings Technology

journal homepage: www.elsevier.com/locate/surfcoat

Full Length Article

Role of magnetic field and bias configuration on HiPIMS deposition of W films

D. Vavassori [a], F. Mirani [a], F. Gatti [a], D. Dellasega [a,b,*], M. Passoni [a,b]

[a] Politecnico di Milano, Dipartimento di Energia, via G. Ponzio 34/3, Milano, Italy
[b] Istituto per la Scienza e Tecnologia dei Plasmi (ISTP) - CNR, via R. Cozzi 53, Milano, Italy

ARTICLE INFO

Keywords:
Tungsten films
HiPIMS
Plasma modeling
Magnetic field
Bias voltage delay
Stress development

ABSTRACT

In this work, the deposition of tungsten (W) films by High Power Impulse Magnetron Sputtering (HiPIMS) has been investigated. By adopting a combined modeling and experimental approach, the role of magnetic field strength and bias configuration on growth of W films has been studied since they are relevant parameters for the energetic and ionized HiPIMS environment. Modeling results showed that increasing the magnetic strength from 40 to 60 mT led to larger W ion fraction in the plasma and, contemporary, to higher ion back-attraction to the target. This, in turn, resulted in a similar W ion fraction in the flux towards the substrate for the two magnetic field strengths considered during the on-time of the voltage pulse. On the contrary, the W ion fraction became significantly different in the afterglow and the same happened to the ion flux composition. Exploiting the studied discharges, W films have been grown applying at substrate negative pulsed bias voltages, both synchronized and delayed to the voltage pulse onset. Films morphology, microstructure, residual stress, composition and density have been examined. In light of plasma differences retrieved from the numerical investigation, film growth and properties are discussed.

1. Introduction

Due to their unique thermophysical, electrical and mechanical properties, tungsten (W) films have application in various industrial and research fields. For instance, W films have been studied for microelectronics industry [1,2], x-ray lithography [3] and surface acoustic wave sensors production [4]. Furthermore, they are also exploited in the energy sector [5–8]. In this respect, W is a key material for the development of magnetic confinement fusion which still presents several aspects to be addressed as, for example, the so-called plasma-wall interaction (PWI). Indeed, W has been extensively studied for the mitigation of PWI [9] and it represents the reference material for the development of the most critical plasma facing components (PFCs), such as the divertor, in ITER [10,11]. Specifically, W films and coatings produced by different deposition methods played a role in various fusion-related applications. For instance, thick W coatings have been exploited as plasma facing materials (PFMs) in tokamaks experiments [7,12,13], while W films have been used to explore specific PWI phenomena expected under fusion-relevant plasma conditions [14–18]. Moreover, W films could be of interest for PFC development in future fusion reactors such as DEMO [10]. Indeed, due to the harsher plasma conditions, the lifetime of ITER-like divertor could be strongly shortened [19,20]. PFCs based on liquid metals are a promising option [21] and liquid tin (Sn) is considered in some designs [22]. In these cases, it is important to prevent the corrosive action on the surfaces in contact with the liquid metal. W films could be a solution for the development of proper protective coatings, thanks to the good resistance to liquid Sn corrosion [23,24].

In this wide framework, conventional physical vapour deposition (PVD) techniques like direct current magnetron sputtering (DCMS) have been mainly considered to grow W films and coatings. The deposition of W films by DCMS is well addressed in the literature [25–30] and, depending on the deposition conditions, films exhibit the α-W phase (bcc structure), the metastable β-W phase (A15-cubic structure) or a mixture of the two. Furthermore, these films are characterized by relatively high internal stresses, usually increasing with thickness, which can lead to film cracking and bad substrate adhesion. Therefore, the presence of a metastable phase and of large internal stresses could represent a limitation for DCMS W films, notably given future fusion-related applications. To overcome the mentioned drawbacks, a possible way is to exploit innovative PVD techniques like high power impulse magnetron

* Corresponding author at: Politecnico di Milano, Dipartimento di Energia, via G. Ponzio 34/3, Milano, Italy.
E-mail address: david.dellasega@polimi.it (D. Dellasega).

https://doi.org/10.1016/j.surfcoat.2023.129343
Received 28 November 2022; Received in revised form 31 January 2023; Accepted 10 February 2023
Available online 18 February 2023

sputtering (HiPIMS) [31,32]. HiPIMS relies on the application of negative voltage pulses (10s–100s μs long) at a low duty cycle to sputter the cathode target. This voltage configuration allows operating at target peak power densities (0.5–10 kW/cm^2) typically two orders of magnitude larger than the time-averaged values. Compared with DCMS, the HiPIMS plasma has a higher density and a higher fraction of ionized sputtered species. Indeed, if in DCMS working gas ions are the main contributors to sputtering, they are not sufficient to generate the high peak currents distinctive of the HiPIMS regime. Thus, part of working gas and/or sputtered species must be recycled [33] to sustain the HiPIMS discharge. This implies that they are ionized and back-attracted to the target during the discharge supporting the sputtering process. Specifically, depending on the most recycled ion species, different HiPIMS discharge modes can be identified [31,34]. The advantage of having a high ionization degree of film-forming species is that their energy and direction can be suitably controlled, for instance applying a proper substrate bias voltage, leading to better quality films. In the last years, many experimental efforts have been made to clarify the action of HiPIMS deposition parameters on the sputtering of different materials [35]. However, only few works exist concerning W films. *Velicu et al.* [36] studied the influence of external magnetic fields and pulse configurations, while *Engwall et al.* [37] and *Shimizu et al.* [38] analyzed the effect of working gas and bias configurations.

On the theoretical side, time-dependent plasma chemical models, such as the Ionization Region Model (IRM), introduced by *Gudmundsson* [39] and *Raadu et al.* [40], offer a deeper insight into complex HiPIMS physics and, in turn, the role of process parameters. Indeed, IRM has been applied to HiPIMS discharges with various materials (e.g. carbon, aluminum, titanium, copper) allowing to explore and to better understand its sophisticated plasma physics [34,35,41–45]. Model and experimental results highlight that the target material and the choice of the deposition parameters are crucial in determining the discharge mode of the HiPIMS process and, in turn, the ionization fraction of the sputtered species [46]. It is worth mentioning that, very recently, IRM developers applied the model to the W discharge in argon atmosphere [47] to examine the discharge voltage influence on the HiPIMS process. The magnetic field strength above the sputtered target (hereinafter *B-field*) is another important process parameter which demonstrated to be strongly relevant for the HiPIMS system. For example, considering titanium discharge, *B-field* showed a significant influence on process characteristics such as ionized flux fraction and deposition rate [43,48,49] or ion energy and distribution [50]. Further studies are needed for a comprehensive understanding of *B-field* action, especially in the case of W as sputtered material. Moreover, experiments considering the influence of this parameter are of great interest since, during HiPIMS operations, its variation is unavoidable due to target erosion [51].

In this study, we propose an integrated approach based on both numerical modeling and experimental investigation of the Ar/W HiPIMS system with focus on two process parameters: the magnetic field strength and the bias voltage configuration. Concerning the former, its influence on plasma parameters behavior was evaluated adapting the IRM to two different Ar/W discharges. Exploiting the studied discharges, it was also investigated the role of synchronized and delayed pulsed substrate bias voltages on W films growth. Their microstructure, morphology, residual stress state, composition and density were examined and compared with model results to evaluate the influence of different plasma conditions and, in turn, process parameters on films. Our results provide new insights into the role of magnetic strength and bias voltage in the deposition of W films with HiPIMS, both in terms of plasma characteristics, film growth and properties.

2. Materials and methods

2.1. Model description

2.1.1. The Ionization Region Model

The Ar/W discharge system was investigated using the Ionization Region Model (IRM), an averaged-volume global model for plasma chemistry. The IRM is a semi-empirical model which implements a set of ordinary differential equations to return the temporal evolution of the plasma species, during and after the pulse, in the so-called Ionization Region (IR). As reported by *Huo et al.* [44], the IR is identified as the dense and bright plasma positioned in the vicinity of the target racetrack. The plasma species are two electron populations (cold and hot), ground state atoms, metastable atoms and ions. The temporal evolution of the *i-th* atomic or ion species is established by considering generation and loss terms related to that species in a balance equation of the form:

$$\frac{dn_i}{dt} = \sum R_i^{generation} - \sum R_i^{loss} \tag{1}$$

where n_i is the *i-th* species density (m^{-3}) and R_i represents the reaction rate (m^{-3}·s^{-1}) of the generation and loss processes included in the model. The density evolution of hot electrons is also followed by a differential equation similar to Eq. (1), while the density of cold electrons is calculated assuming the quasi-neutrality approximation (coherent with HiPIMS discharges [44]). The rate equation describing the energy density evolution of cold electrons is written as:

$$\frac{dT_e}{dt} = \sum Q_{abs} - \sum Q_{loss} \tag{2}$$

where T_e (eV) is the cold electrons temperature, while Q_{abs} and Q_{loss} (eV·s^{-1}) are related to the power absorbed and lost by the plasma due to different processes, respectively.

Being semi-empirical, the model requires several input parameters that depend on the experimental system (e.g., gas pressure, geometry, sputter yields) and the experimental discharge current $I_D(t)$. The model is constrained to reproduce the measured $I_D(t)$ using two unknown fitting parameters [44]. The first fitting parameter is the back-attraction probability of ionized species towards the cathode β, and the second is the fraction of the discharge voltage U_D across the IR $f = U_{IR}/U_D$. It is worth mentioning that the magnetic field does not represent an input parameter for the IRM, but it is taken into account indirectly by using as input the measured $I_D(t)$ [43].

The calculated current I_{calc} is computed using the flux of the *i-th* charged species towards the racetrack Γ^{RT}:

$$I_{calc} = e \sum S_{RT} Z_i \Gamma_i^{RT} \left(1 + \gamma_{eff_i}\right) \tag{3}$$

where e is the elementary charge, S_{RT} is the racetrack area, Z_i is the charge number of the *i-th* ionized species and γ_{eff} is effective secondary electron emission yield of the *i-th* ionized species (see Section 2.1.2). This value must reproduce at best the input experimental current $I_D(t)$. In this respect, we performed a fitting procedure over a 2-dimensional space parameter (β, f) by applying a least square method to minimize a figure of merit which in this work has been defined as:

$$X = \int_{pulse} \left| \frac{I_{calc}(t) - I_D(t)}{I_D(t)} \right| dt. \tag{4}$$

Using this approach, the best fit was determined by varying β in the interval 0.5–1 and f in the interval 0.01–0.2 and choosing the (β, f) couple which provides the minimum X.

2.1.2. IRM application to the Ar/W system

Ten populations are included in our model: cold and hot electrons (e^C, e^H), ground state argon atoms, metastable argon atoms (Ar^m), singly charged argon ions (Ar^+), tungsten atoms (W), singly and doubly

charged tungsten ions (W^+, W^{2+}). Specifically, ground state argon atoms are further divided according to their kinetic energy. Cold argon atoms (Ar) are ground state atoms at room temperature. Hot argon atoms (Ar^H) are ground state atoms which immediately return from the target after argon ion impact with energy around a few eV, while warm argon atoms (Ar^W) are ground state atoms which implant in the target after argon ion impact, return to the target surface and leave with an energy around 0.1 eV. Details about the geometry and equations used in the model can be found in Appendix A.

All the reactions and rate coefficients implemented in the IRM are shown in Table 1. For argon-electron reactions, we used rate coefficients calculated in previous works. Instead, as far as electron-metal and argon-metal reactions are concerned, rate coefficients were obtained starting from literature data (both experimental and theoretical). For cold and hot electrons, rate coefficients were calculated assuming a Maxwellian energy distribution in the 1–10 eV and 200–1000 eV ranges, respectively.

Rate coefficients for electron-impact ionization, excitation and elastic scattering of W atoms were derived using the data from *Blanco et al.* [53]. The 10 lowest excited levels of W were considered to determine an average energy threshold for the excitation reaction. Then, the method reported in [58] was applied to evaluate the excitation cross section of each level. Subsequently, the average energy threshold is estimated by summing the values of each energy level weighted by the ratio between the corresponding cross section and the total one. The data of *Stenke et al.* [59] and *Vainshtein et al.* [55] were used to calculate the rate coefficient for electron-impact ionization of W^+ ions. The cross section for Penning ionization was estimated using published values for other elements [56,60–62] and performing a linear scaling through an empirical formula reported in the literature [56]. Then, the rate coefficient for W species was calculated assuming an average energy equal to half the surface binding energy (see below). Instead, for charge exchange between argon and tungsten species the rate coefficient experimentally retrieved for iron (Fe) [57] was considered. Indeed, in previous theoretical works [63,64], it is argued that Fe and W should have similar behavior concerning charge transfer with Ar^+ ions. We used the fits reported by *Anders et al.* [65] for the sputter and self-sputter yields. There, the yield is approximated by the allometric function $Y = aE_i^b$, where E_i is the energy of the impinging ion and a and b are constants depending on the ion-target system. E_i is equal to the discharge voltage; thus, the sputter yield follows its time evolution. In our case for Ar sputtering, $a = 0.0429$ and $b = 0.521$, while $a = 0.0066$ and $b = 0.77$ for self-sputtering. As already mentioned, we assumed that sputtered atoms have average energy equal to half the surface binding energy (8.9 eV for W) since the energy spectrum of sputtered species peaks around this value [41]. Relying on literature data [66,67], the secondary electron emission yield related to impinging Ar^+ ions $\gamma_{Ar}{}^+$ was set equal to 0.1 by considering a clean target [68]. $\gamma_W{}^+$ was assumed 0, while $\gamma_W{}^{2+}$ was calculated using the formula reported in [33]. The secondary electron recapture probability r was fixed to 0.7 [69,70]. Thus, the effective secondary electron emission yields were calculated as $\gamma_{eff} = \gamma \cdot (1 - r)$.

2.2. Experimental details

The magnetron sputtering system described in [71] was equipped with two circular W targets (diameter = 76 mm) with nominal thicknesses of 3 mm and 6 mm. In this way, different magnitudes of *B-field* at the target surface were achieved. As detailed in Appendix B, the magnetic field associated with our magnetron source was retrieved with magnetostatic Finite Element Method. Considering the position of the race-track and its depth, the average intensity at target surface resulted of about 60 mT for the thinner target and 40 mT for the thicker one. Hereinafter, BF60 will refer to the configuration with the higher field, while BF40 to the one with the lower field.

W films were deposited onto single side 500 μm thick (100) silicon (Si) wafers (2 × 2 cm^2 in size) cleaned using isopropanol. Prior each deposition, the vacuum chamber was evacuated to a base pressure lower than 5×10^{-4} Pa and then filled with Ar (99.999 % purity) with a constant inlet gas flow rate of 80 sccm and pressure equal to 0.5 Pa. For both *B-field* conditions, HiPIMS pulse length was set to 100 μs. The resulting discharge voltage and current waveforms were acquired by a Rigol DS4034 oscilloscope working in average mode. The main process parameters adopted for the two configurations are reported in Table 2.

Since the discharge voltage was kept approximately constant at 900

Table 1
Reactions, energy thresholds and rate coefficients implemented in the IRM. For each electron impact reaction, the first rate coefficient refers to cold electrons and the second to hot electrons.

Reaction	Energy Thr. [eV]	Rate Coefficient k [m^3/s]	Ref.
$Ar + e \rightarrow Ar^+ + 2e$	15.76	$k^C_{iz,\,Ar} = 2.34 \times 10^{-14} T_e^{0.59} \exp(-17.44/T_e)$ $k^H_{iz,\,Ar} = 8 \times 10^{-14} T_e^{0.16} \exp(-27.53/T_e)$	[44]
$Ar^m + e \rightarrow Ar^+ + 2e$	4.2	$k^C_{iz,\,Ar^m} = 6.8 \times 10^{-15} T_e^{0.67} \exp(-4.2/T_e)$ $k^H_{iz,\,Ar^m} = 5.7 \times 10^{-13} T_e^{-0.33} \exp(-6.82/T_e)$	[44]
$Ar + e \rightarrow Ar^m + e$	11.56	$k^C_{ex,\,Ar} = 2.5 \times 10^{-15} T_e^{0.74} \exp(-11.56/T_e)$ $k^H_{ex,\,Ar} = 3.85 \times 10^{-14} T_e^{-0.68} \exp(-22/T_e)$	[44]
$Ar^m + e \rightarrow Ar + e$	−11.56	$k^C_{dex,\,Ar^*} = 4.3 \times 10^{-16} T_e^{0.74}$ $k^H_{dex,\,Ar} = 4.3 \times 10^{-16} T_e^{0.74} +$ $4.957 \times 10^{-14} T_e^{-0.39} \exp(-7.78/Te) + 2.67 \times 10^{-15}$	[44]
$Ar + e \rightarrow Ar + e$	–	$k_{el,\,Ar} = 2.33 \times 10^{-14} T_e^{1.609} \exp(0.0618$ $\times(\ln(T_e))^2 - 0.1171 \times (\ln(T_e))^3)$	[52]
$W + e \rightarrow W^+ + 2e$	7.98	$k^C_{iz,\,W} = 1.78 \times 10^{-13} T_e^{0.181} \exp(-12.095/T_e)$ $k^H_{iz,\,W} = 5.78 \times 10^{-13} T_e^{-0.083} \exp(-28.2/T_e)$	[a]
$W + e \rightarrow W^* + e$	0.65	$k^C_{ex,\,W} = 9.15 \times 10^{-13} T_e^{-0.43} \exp(-9.034/T_e)$ $k^H_{ex,\,W} = 2.23 \times 10^{-13} T_e^{0.023} \exp(-7.55/T_e)$	[a]
$W + e \rightarrow W + e$	–	$k_{el,\,W} = 10^{(-16.94+1.403\times\ln(T_e)-0.106\times(\ln(T_e))^2)}$	[a]
$W^+ + e \rightarrow W^{2+} + 2e$	16.3	$k^C_{iz,\,W^+} = 6.63 \times 10^{-14} T_e^{0.25} \exp(-16.72/T_e)$ $k^H_{iz,\,W^+} = 4.053 \times 10^{-11} T_e^{-0.94} \exp(-163.309/T_e)$	[b]
$Ar^m + W \rightarrow Ar + W^+ + e$	3.58	$k_P = 1.48 \times 10^{-15}$	[c]
$Ar^+ + W \rightarrow Ar + W^+$	–	$k_{chexc} = 7.6 \times 10^{-15}$	[d]
$Ar + W^{2+} \rightarrow Ar^+ + W^+$	–	$k_{chexc,\,2} = 7.6 \times 10^{-15}$	[d]

[a] Calculated from the cross section in [53].
[b] Calculated from the cross section in [54,55].
[c] Estimated with the empirical formula in [56].
[d] Estimated with the experimental data in [57].

Table 2
Process parameters considered for films deposition.

	BF40	BF60
B-field (average) [mT]	~40	~60
Pressure [Pa]	0.5	0.5
Pulse length [μs]	100	100
Frequency [Hz]	175	175
Duty cycle [%]	1.75	1.75
Discharge voltage [V]	~900	~900
Average discharge power [W]	210–230	620–640
Peak current density [A/cm^2]	0.6–0.8	1.8–2

Substrate bias voltage		
Configuration	Negative pulse Synchronized/delayed	Negative pulse Synchronized/delayed
Bias pulse length [μs]	100	100
Bias pulse amplitude [V]	200, 400, 800	400, 800
Bias pulse delay [μs]	0, 60, 100	0, 60

V, the average discharge power resulted considerably different in the two examined *B-field* configurations. Thus, to obtain films with a comparable thickness in the range 400–500 nm both with 40 mT and 60 mT field strengths, the deposition time was set to 90 and 45 min, respectively. For both *B-field*, one goal of the depositions was to evaluate the effect of negative 100 μs long pulsed bias with negative bias voltage amplitudes (hereinafter indicated with U_S) on the final film properties. For the BF40 configuration, U_S was set equal to 200, 400 and 800 V while, for the BF60 configuration, equal to 400 and 800 V. It should be noted that, for the thickness range considered, the chosen process parameters resulted in film failure if the substrate was left in floating conditions or lower bias voltage amplitudes were applied. In addition, we considered the effect of a bias delay $\Delta\tau$ with respect to the pulse onset. For both configurations, a synchronized bias ($\Delta\tau = 0$ μs) and a delayed bias ($\Delta\tau = 60$ μs) were examined. Moreover, a second bias delay time ($\Delta\tau = 100$ μs) was investigated for the BF40 configuration.

Crystalline phase and crystallographic orientation of the films were evaluated through X-Ray Diffraction (XRD) analysis performed by a Panalytical X'Pert PRO X-ray diffractometer in $\theta/2\theta$ configuration. Film thickness and morphological properties were assessed by a Zeiss Supra 40 field emission Scanning Electron Microscopy (SEM), operating at an accelerating voltage of 5 kV. The same system, operating at an accelerating voltage of 5 and 10 kV, was exploited to perform Energy Dispersive X-Ray Spectroscopy (EDXS) to analyze film composition. Residual stresses were measured by an optical implementation of the wafer curvature method [71] and calculated according to the Stoney equation [72]. Lastly, a sensitive analytical balance (10^{-5}g) was used to weigh samples before and after depositions and to estimate the film density.

3. Results

3.1. Model results

As mentioned before, we investigated the W/Ar HiPIMS discharge taking as input parameters of the model the experimental waveforms acquired during film depositions. In both *B-field* configurations the discharge voltage was fixed at the approximately constant value of 900 V. Further details related to other process parameters are resumed in Table 2.

The two experimental current waveforms I_D are reported in Fig. 1(a). For the BF40 configuration, I_D is characterized by an initial peak. Then, due to the depletion of working gas, a decay follows down to an approximately constant plateau at about 12–13 A until the end of the pulse. A different behavior can be observed for the BF60 configuration. After the initial peak, I_D shows a short decrease followed by a growth that reaches a stable plateau, at 38 A, near the end of the pulse.

Fig. 1(b) and (c) show the experimental and the corresponding modeled discharge current in the two *B-field* configurations. Moreover, the current composition at the target surface is also reported. In the BF40 configuration the best fit was found for $\beta = 0.81$ (ion back-attraction probability) and $f = 0.049$ (fraction of the total discharge voltage across IR), while in the BF60 configuration for $\beta = 0.88$ and $f = 0.053$. It is reasonable that the fit parameter β is smaller for the BF40 configuration than for the BF60 one since the back-attraction probability is lowered when the magnetic field strength is reduced [46]. Fig. 1(b) displays that Ar^+ ions provide a primary contribution to the peak in the initial trend of the discharge current in the BF40 configuration. However, after approximately 20 μs, Ar^+ ions contribution decreases due to the working gas rarefaction effect generated by the "sputter wind" [35]. Concurrently, W^+ ions contribution increases and then dominates the discharge until the end of the pulse, roughly representing 65 % of the current. Instead, Ar^+ contribution settles around a constant value accounting for <35 % of the current. The contributions of W^{2+} ions and of secondary electrons (I_{SE}) are much smaller for the entire duration of the discharge. As displayed in Fig. 1(c), also in the BF60 configuration, W^+ ions become the dominant species until the end of the pulse. Nonetheless, in this case, the relative contribution to the current is more pronounced, approximately 80 % for W^+ ions and 20 % for Ar^+ ions. Again, W^{2+} ions and secondary electrons contributions are negligible.

Furthermore, in Fig. 1(b) and (c), a grey dashed-dotted line indicates

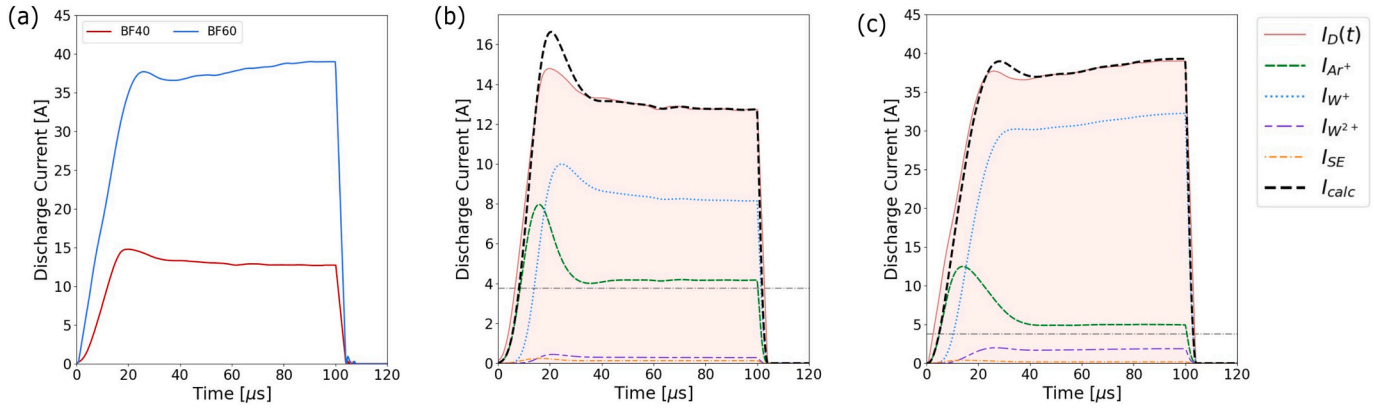

Fig. 1. (a) The temporal evolution of the experimentally acquired discharge currents for both *B-field*. (b–c) The discharge current calculated by IRM and its composition at the target surface for BF40 and BF60 configurations, respectively. The horizontal grey dashed-dotted lines in panels (b) and (c) represent the I_{crit} value. The legend on the right refers to (b) and (c) panels. I_D and I_{calc} are the experimental and calculated currents. $I_{Ar}{}^+$, $I_W{}^+$, $I_W{}^{2+}$ and I_{SE} are the contributions of Ar^+ ions, W^+ ions, W^{2+} ions and secondary electrons, respectively.

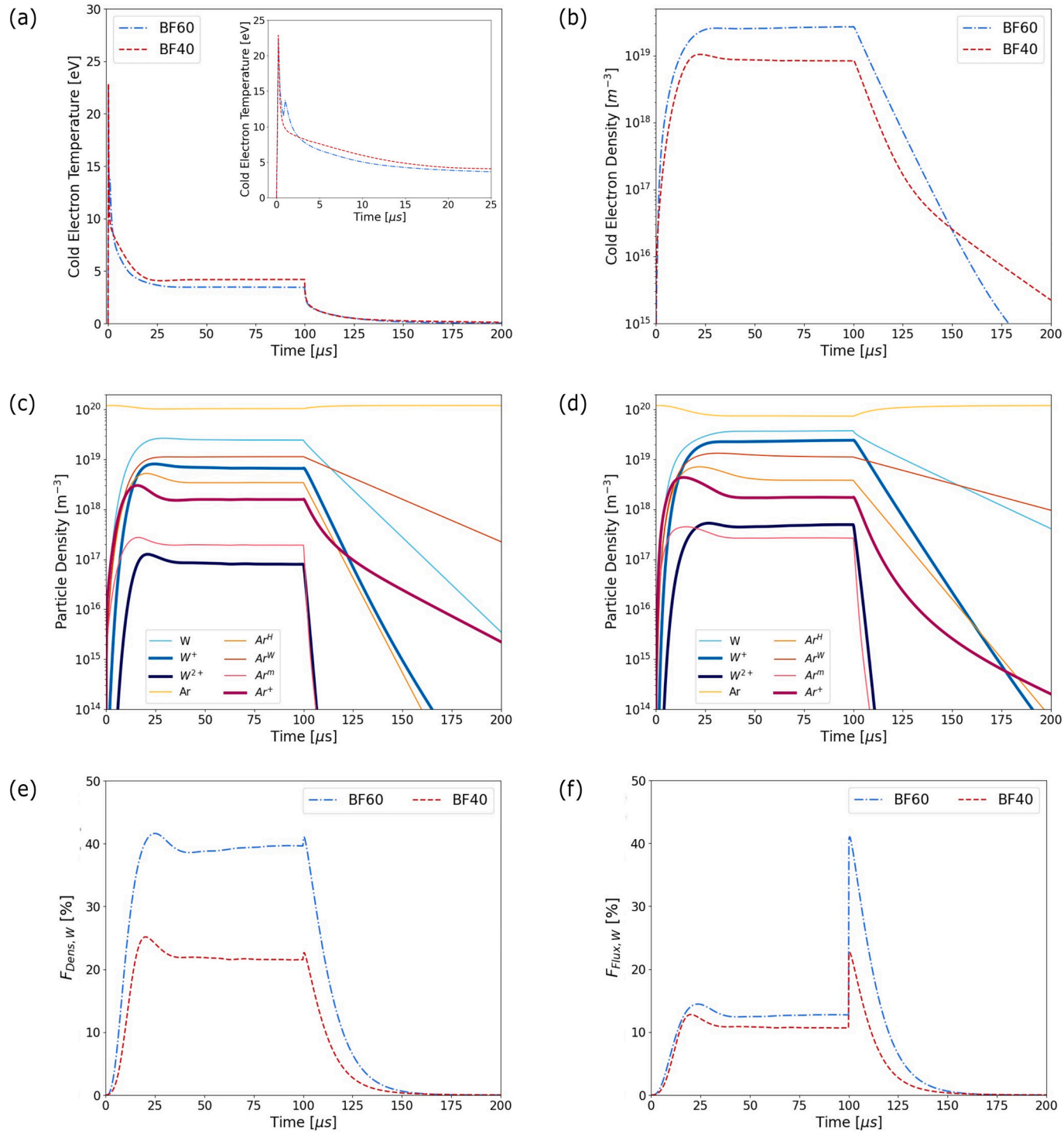

Fig. 2. The temporal evolution of (a) cold electron temperature and (b) cold electron density in the IR for both BF40 and BF60 configurations. The temporal evolution of particle density in the IR for BF40 (c) and BF60 (d) configurations. The ionized species densities are represented with thicker lines. For W sputtered species: the evolution of the ionized fraction (e) in the IR and (f) in the flux from the IR.

the so-called critical current I_{crit}, which represents the upper limit for the argon ion current considering the ionization of all incoming argon atoms and no recycling mechanism. I_{crit} is calculated according to the formula proposed by *Huo et al.* [73] resulting equal to 3.77 A for both discharges. The Ar^+ contribution results slightly larger than this value suggesting a small recycling of working gas.

Fig. 2 presents the main model results related to the temporal evolution of plasma species in the IR. Fig. 2(a) and (b) illustrate the cold electron temperature T_e and density n_e^C of the Ar/W HiPIMS system for the *B-field* configurations examined. For both cases, in the early stage of the pulse, T_e is characterized by a sharp peak which rapidly decreases (see the inset in Fig. 2(a)). As explained in [45], the high temperatures in the first microseconds of the discharge are related to physical (presence of a limited number of electrons absorbing the input power) and modeling (underestimation of plasma density) reasons. This, in turn, is reflected in the initial different values of I_{calc} and $I_D(t)$, as shown in Fig. 1

(b) and (c). After the initial peak, in the BF60 condition, T_e stabilizes approximately at 3.5 eV during the pulse. On the contrary, in the BF40 case, T_e decreases and reaches a minimum value of about 4 eV. Then, it slowly increases up to 4.2 eV at the end of the pulse. Fig. 2(b) shows the n_e^C temporal evolution. Its trend is similar to the one of discharge current since its variation influences the ion generation and, in turn, the current on target. Increasing *B-field* from 40 mT to 60 mT, n_e^C passes from 8.5 $\times$ 10^{18} m^{-3} to 2.6 $\times$ 10^{19} m^{-3} during the stable period of the pulse. We observed a reasonable opposite behavior of T_e and n_e^C for the two *B-field* configurations. Indeed, a higher n_e^C implies an amplified sputtering process and, thus, a higher number of electron-atom impact ionization events. This results in an enhanced electron cooling and, in turn, a lower T_e.

Fig. 2(c) and (d) display the temporal evolution of particle densities for BF40 and BF60 configurations, respectively. The ground state argon atoms are the main species during the HiPIMS discharge in both configurations. Their densities are characterized by an initial decrease indicating working gas rarefaction. Successively, n_{Ar} settles around a constant value in the BF40 case, while in the BF60 case continues to decrease but more gradually. The other argon species exhibit a similar trend in the two configurations during the pulse. Specifically, hot and warm argon atoms returning from the target show comparable values, while metastable argon atoms (negligible compared with other species) are smaller in the 40 mT condition. W atoms have the second largest density during the discharge. Their density shows a steep increase lasting a few tens of μs. Successively, it stabilizes in both *B-field* conditions. As it might be expected, n_W is larger in the BF60 configuration. Concerning the ionized species density evolution, at the beginning of the pulse Ar^+ ions represent the main contribution. However, after about 10 μs, the W^+ ion density overcomes the Ar^+ one in both configurations. Until the end of the pulse, they remain the dominant ionized species. More precisely, during the plateau phase of the pulse, n_{W^+} is approximately four times n_{Ar^+} in the BF40 configuration. Then, only in the afterglow ($t \simeq 120$ μs) the situation is reversed. In the BF60 configuration, n_{W^+} is one order of magnitude larger than n_{Ar^+}. Again, this condition changes only in the afterglow, but with longer times ($t \simeq 175$ μs). In all cases, the density of W^{2+} species is approximately two orders of magnitude smaller than the singly charged one.

Fig. 2(e) and (f) show the W ion fraction in the IR ($F_{Dens,W}$) and in the flux towards the diffusion region ($F_{Flux,W}$), respectively. The two quantities are calculated according to [74], exploiting both previously reported results and other parameters extracted from the model. Fig. 2(e) displays that a decrease in *B-field* results in lower $F_{Dens,W}$ during the on-time of the pulse, in agreement with precedent works [44,49].

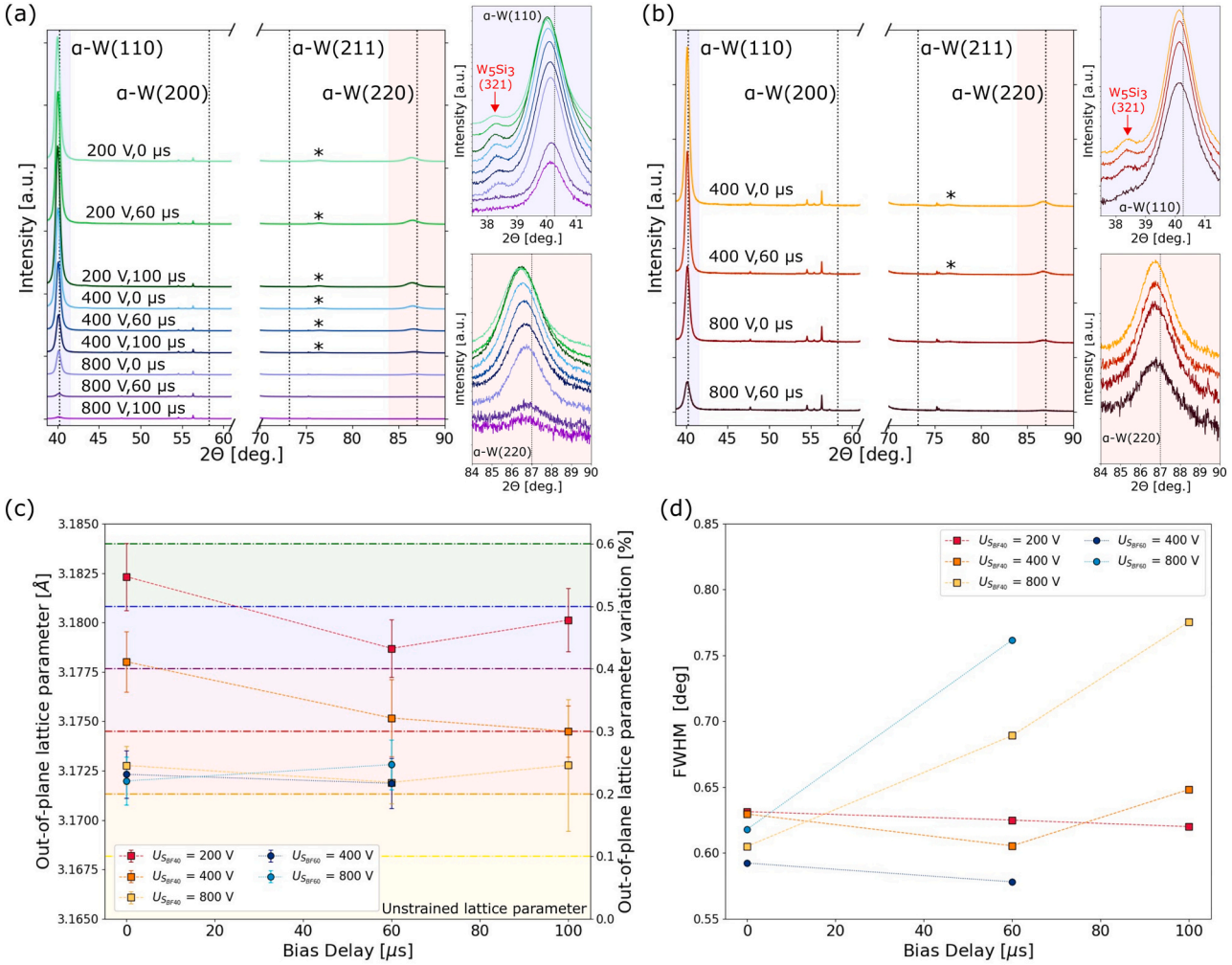

Fig. 3. X-ray diffractograms for: (a) films deposited with U_S = 200, 400, 800 V, $\Delta\tau$ = 0, 60, 100 μs in the BF40 configuration and (b) films deposited with U_S = 400, 800 V, $\Delta\tau$ = 0, 60 μs in the BF60 configuration. For both (a) and (b) panels the peak indicated with (*) is identified as a Cu K-β peak due to the XRD source. The narrow peaks not explicitly marked by symbols or vertical lines are related to the Si substrate. Lateral panels: magnification of the 37.5°–41.5° and 84°–90° ranges (logarithmic scale on the vertical axis). The red arrow indicates the (321) reflection of W_5Si_3. (c) α-W cubic out-of-plane lattice parameter as a function of the bias voltage delay. The right y-axis indicates the percentage change from the unstrained bulk value. (d) Evolution of the FWHM calculated from the peak of α-W (110) as a function of the bias voltage delay.

Moreover, Fig. 2(f) evidences that $F_{Flux,W}$ has similar values for the two configurations during the voltage pulse on-time. On the other hand, at the end of the pulse, a slight increase for $F_{Dens,W}$ and a sharp increase for $F_{Flux,W}$ can be noted.

3.2. Experimental results

In the following, details related to the properties of W films deposited exploiting the HiPIMS pulses analyzed in Section 3.1 are reported. As already stated, in addition to the influence of magnetic field, we considered the effect of different substrate bias voltage configurations on films growth. In light of modeling results, film properties will be examined in Section 4.

3.2.1. XRD analysis

To investigate the microstructure evolution of W films, X-ray diffractograms were acquired. Fig. 3 presents the results of this analysis. Only peaks related to the α-phase of W have been recognized. Fig. 3(a) shows the XRD patterns of W films grown exploiting the BF40 configuration. The peak related to the (110) reflection is always present and it is the most intense one. In addition, the peak associated with the (220) reflection is visible. Both signals are downshifted to the nominal bulk value by $2\Theta = 0.1°–0.25°$, suggesting the presence of internal stresses in the films. No peaks related to the (200) and to the (211) reflections can be observed. The small peak preceding the one of the (110) reflection, visible in some patterns of the first lateral panel of Fig. 3(a) and indicated by a red arrow, is identified as the (321) reflection of W_5Si_3 [75]. Fig. 3(b) shows the XRD patterns of W films grown exploiting the BF60 configuration. As in the previous case, only the (110) and (220) reflections are present and the small speak related to the (321) reflection of W_5Si_3 is visible (indicated by a red arrow in the first lateral panel of Fig. 3(b)). The detected W peaks are downshifted by $2\Theta = 0.06°–0.15°$ with respect to the expected bulk value, again indicating the presence of residual stresses in the films.

The α-W cubic out-of-plane lattice parameter of the deposited films is represented in Fig. 3(c) as a function of the bias delay. The left y-axis shows the values calculated from the position of the diffraction peaks of the (110) and (220) reflections, while the right one indicates its relative variation with respect to the unstrained bulk value. For the BF40 configuration and $U_S = 200$, 400 V, the out-of-plane lattice parameter reduces as the bias delay increases with deviation from the bulk value always larger than 0.3 %. Specifically, considering $U_S = 200$ V, the minimum lattice parameter value is observed for $\Delta\tau = 60$ µs, while, for $U_S = 400$ V, it decreases monotonically with bias delay. Differently, examining $U_S = 800$ V case, the lattice parameter remains approximately constant moving from $\Delta\tau = 0$ µs to $\Delta\tau = 100$ µs, resulting in a

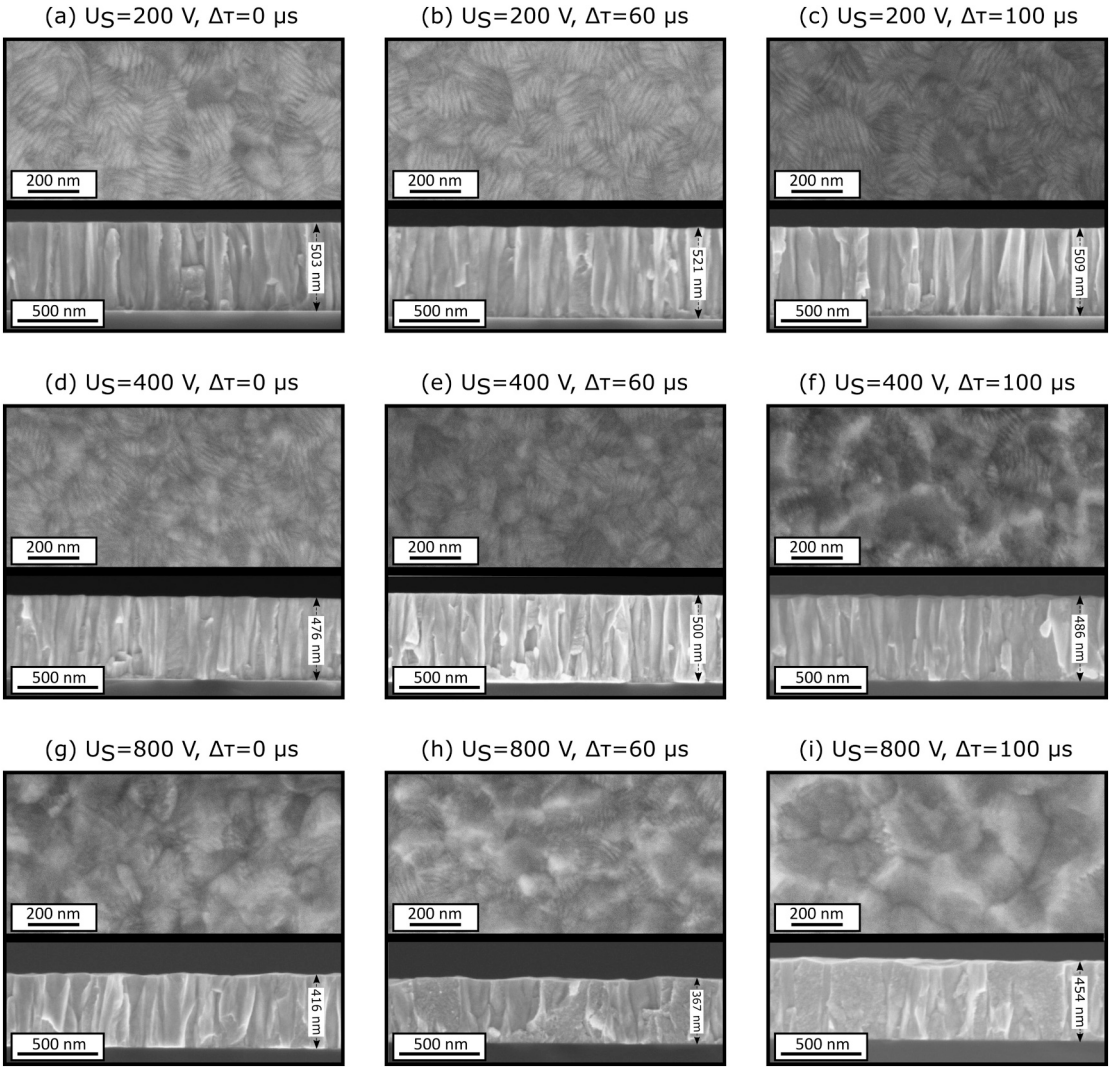

Fig. 4. Morphology evolution of W films deposited in BF40 configuration. SEM images of films grown with: (a–c) $U_S = 200$ V and $\Delta\tau = 0$, 60, 100 µs; (d–f) $U_S = 400$ V and $\Delta\tau = 0$, 60, 100 µs; (g–i) $U_S = 800$ V and $\Delta\tau = 0$, 60, 100 µs.

variation from the bulk value in the range 0.22–0.25 %. On the other hand, if BF60 configuration is considered, the out-of-plane lattice parameter seems to remain constant independently from the U_S and $\Delta\tau$ values analyzed. As a consequence, the variation with respect to the bulk value always lies in the 0.22–0.25 % range.

The evolution of the full width at half maximum (FWHM) of α-W (110) peak is plotted in Fig. 3(d) as a function of $\Delta\tau$. If $\Delta\tau = 0$ μs, FWHM is characterized by a nearly constant value in the range 0.59°–0.63° considering all investigated films. In both *B-field* configurations, by increasing $\Delta\tau$, a significant increment in FWHM is observed if $U_S = 800$ V. Instead, for other U_S values examined, the FWHM variation with $\Delta\tau$ increase results less marked.

3.2.2. Morphological characterization with SEM

The morphological characteristics of W films are displayed in the panels of Figs. 4 and 5. Each panel shows a planar view SEM image in the upper part. In the lower part, a cross-section image is reported together with the measured average thickness. In BF40 configuration, for $U_S =$ 200 V, W films always exhibit a "nano-ridged" surface characterized by elongated and streaked structures, as shown in the top part of Fig. 4 (a–c). This leads to a densely packed grain structure formation, as confirmed by cross-section images (bottom part of Fig. 4(a–c)) displaying a compact columnar growth. Likely, this is related to the highly textured nature of the films along the (110) direction of the α-W phase, as confirmed by XRD measurements and as reported in precedent works [38,76]. For $U_S = 400$ V and 800 V, the "nano-ridged" pattern progressively diminishes, as visible in the top part of Fig. 4(d–f) and (g–i), respectively. Specifically, the film surface appears more uniform as $\Delta\tau$ is increased, probably under the action of different processes (e.g., grain coarsening, grain growth, etching and re-sputtering). The cross-section images (bottom part of Fig. 4(d–f) and (g–i), respectively) again show a columnar growth. Increasing U_S, columns size appears widened, in agreement with a grain coarsening hypothesis, and films thickness decreases independently of bias delay.

Fig. 5 illustrates the morphology of W films deposited in BF60 configuration. Fig. 5(a) refers to a delaminated film grown with $U_S =$ 200 V and $\Delta\tau = 0$ μs. As in the BF40 configuration, SEM images reveal a densely packed grain structure characterized by a "nano-ridged" surface. Considering $U_S = 400$ V and $\Delta\tau = 0$ and 60 μs, the presence of the "nano-ridged" pattern can be again identified, as shown in the top part of Fig. 5(b) and (c). However, compared to the corresponding BF40 configuration films (top part of Fig. 4(d) and (e)), the pattern reduction seems to be more evident. For $U_S = 800$ V and $\Delta\tau = 0$ and 60 μs, planar images suggest a significant re-sputtering effect. Indeed, the top parts of Fig. 5(d) and (e) exhibit superficial features similar to the ones of nanostructured W coatings exploited in plasma irradiation experiments [16]. In all cases, cross section images (bottom parts of Fig. 5(d) and (e)) exhibit a columnar growth for the films. Again, for increasing values of U_S, films thickness decreases.

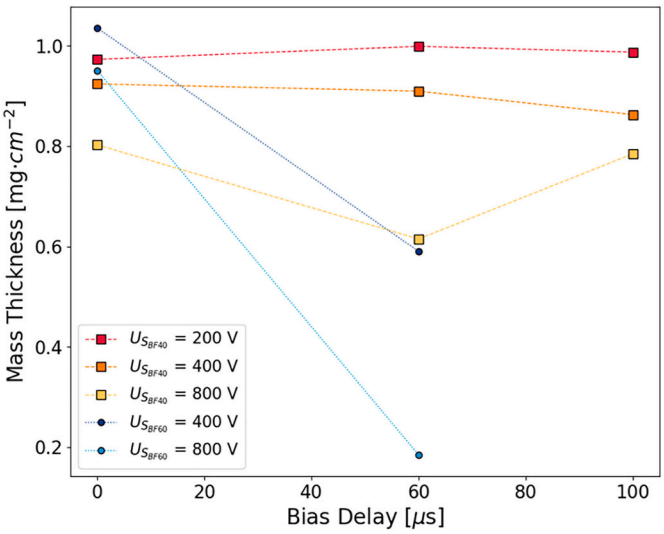

Fig. 6. Evolution of films mass thickness versus bias delay, as the magnetic field strength and the bias value are varied.

For both BF40 and BF60 configurations, Fig. 6 displays films mass thickness as a function of the bias delay. Independently on magnetic field strength and on bias value, the mass thickness varies in the range 0.8–1 mg·cm^{-2} if $\Delta\tau = 0$ μs. For the 40 mT case, a bias pulse time-shift has little effects on the mass thickness for $U_S = 200$ and 400 V. Instead,

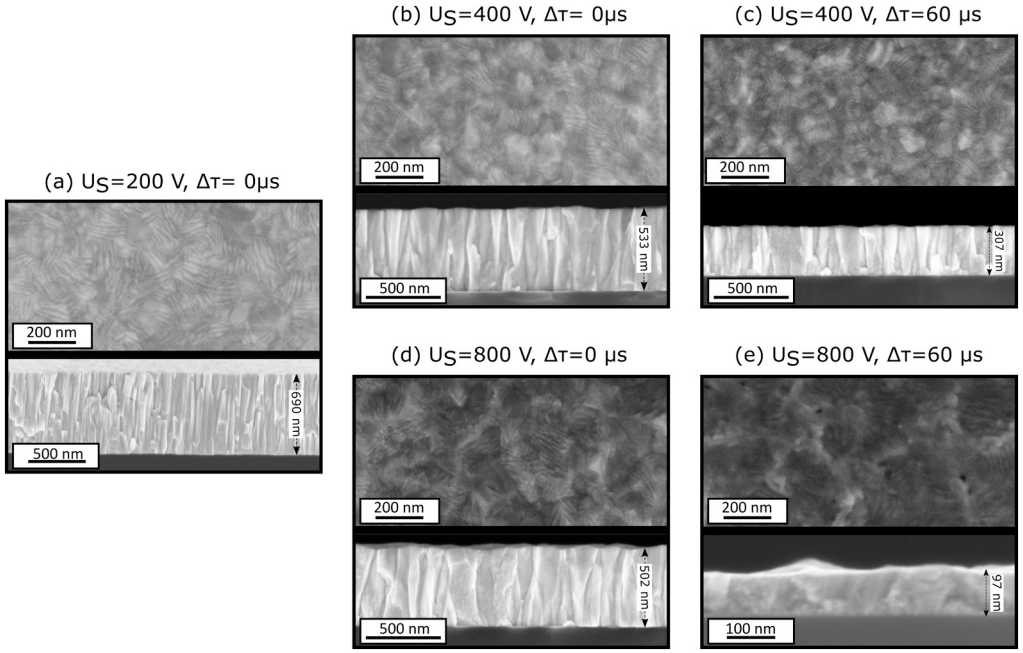

Fig. 5. Morphology evolution of W films deposited in BF60 configuration. SEM images of film grown with: (a) $U_S = 200$ V and $\Delta\tau = 0$ μs; (b–c) $U_S = 400$ V and $\Delta\tau =$ 0, 60 μs; (d–e) $U_S = 800$ V and $\Delta\tau = 0$, 60 μs.

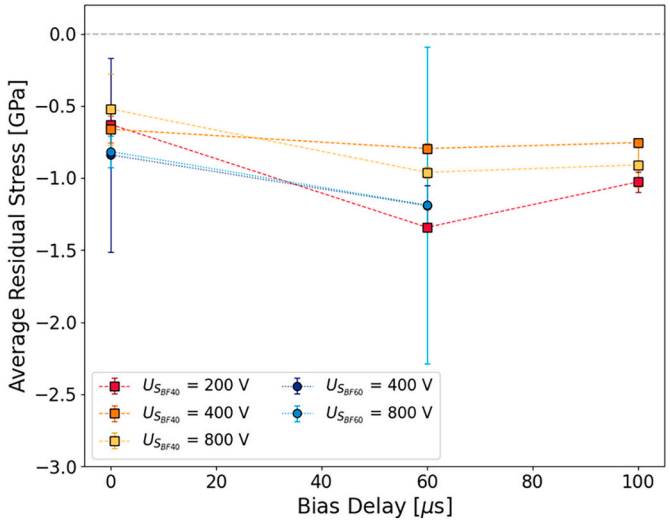

Fig. 7. Evolution of films average residual stress versus bias delay, as the magnetic field strength and the bias value are varied.

for U_S = 800 V, a mass thickness decreases down to 0.6 mg·cm^{-2} is observed only for $\Delta\tau$ = 60 μs. Differently, for films deposited with 60 mT intensity, a bias pulse time-shift results in a strong mass thickness reduction down to approximately 0.6 mg·cm^{-2} for U_S = 400 V and 0.2 mg·cm^{-2} for U_S = 800 V, again highlighting an enhanced re-sputtering effect for this configuration.

3.2.3. Stress analysis by substrate curvature method

The average residual stresses of deposited films are reported in Fig. 7 as a function of bias voltage delay. For both *B-field* conditions, a bias switch from synchronous ($\Delta\tau$ = 0 μs) to delayed ($\Delta\tau$ = 60 and 100 μs) induces higher compressive stresses. Specifically, for BF40 configuration, a maximum increase up to −1.35 GPa is noted for U_S = 200 V and $\Delta\tau$ = 60 μs. Also in the U_S = 400 and 800 V cases an increment in compressive stress is observed. However, compared to the previous situation, a sort of stable condition seems to be reached while delaying the bias pulse. Moving to the BF60 case, the delayed bias configuration leads to an increase of average residual stress. Moreover, with respect to the corresponding BF40 films, higher average compressive stresses have been measured.

3.2.4. Films composition and density

The Ar fraction in the films is displayed in Fig. 8(a). For the BF40 configuration, the Ar content is negligible for all bias delay if U_S = 200 V. Fixing U_S to 400 and 800 V leads to an increase of Ar fraction in the films, particularly marked for the largest bias value.

For the BF60 configuration, considering U_S = 400 and 800 V, a bias pulse time-shift results in a Ar content increase but to a lower extent with respect to the corresponding deposition conditions with a *B-field* equal to 40 mT. Fig. 8(b) shows the density evolution for the *B-field* and the different substrate bias conditions examined. For $\Delta\tau$ = 0 μs, all films are characterized by a density near the bulk one, independently on the specific deposition condition. For the BF40 configuration, a bias pulse time-shift results in nearly constant film density if U_S = 200 V, while a significant decrease up to approximately 17–18 g·cm^{-3} is visible if U_S is set to 400 and 800 V. Differently, increasing the bias delay, films grown with the BF60 configurations exhibit only a small density reduction for both U_S = 400 and 800 V.

4. Discussion

Among deposition parameters, the magnetic field strength above the racetrack has a significant impact on the HiPIMS discharge physics. For a given input voltage, an increment in the magnetic field leads to larger currents due to a more efficient discharge which, in turn, enables more ionization [44,49]. The presented results indicate that this mechanism applies also to the studied Ar/W HiPIMS discharge. As seen in Fig. 1(a), the magnetic field is crucial in determining discharge current values and the associated waveform shapes. The shape evolution suggests that the magnetic field influences the HiPIMS operation mode during the plateau phase, as reported for other target materials [77]. Modeling results support this hypothesis. For the two magnetic field configurations, during the plateau phase, we found that W^+ ions dominate the total ion current to the target (see Fig. 1(b) and (c)) but with different contributions. This variation can be attributed to a different degree of self-sputtering induced in the discharge by the magnetic field strength. Thus, to have a more quantitative analysis of the recycling process characterizing the examined W discharges, we decided to follow the detailed approach proposed in *Brenning et al.* [34]. Indeed, the IRM allows distinguishing between the primary current I_{prim}, constituted by the working gas atoms ionized for the first time, and the recycled currents I_{SS} and $I_{gas-recycle}$ carried by recycled metal ions and recycled gas ions, respectively. If the ratio of I_{prim} to the total discharge current I_D is smaller than 0.5, the discharge is dominated by recycling. In the examined discharges, during the plateau phase of the pulse (approximately after t

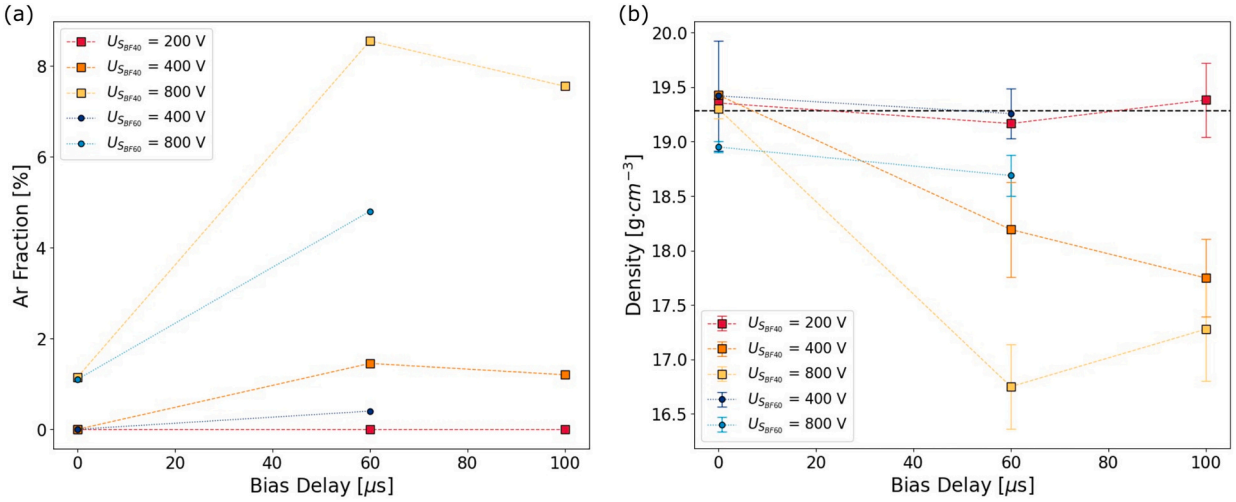

Fig. 8. Evolution of (a) Ar atomic fraction and (b) density of W films versus bias delay, as the magnetic field strength and the bias value are varied. In panel (b), the black dashed line represents the W bulk density.

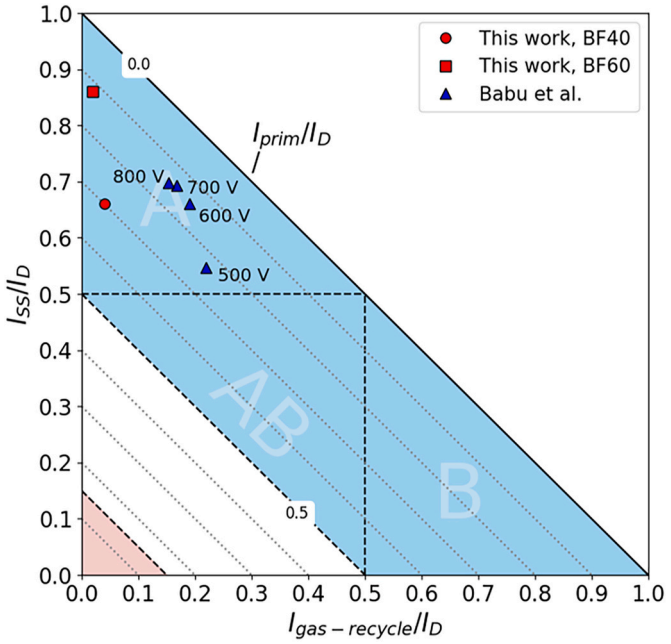

Fig. 9. Recycling map for the Ar/W HiPIMS system. The circular and square red points represent the discharges examined in this work. The triangular blue points represent the discharges analyzed by *Babu et al.* [47]. The respective discharge voltages are indicated in the figure.

= 30 μs), I_{prim}/I_D is about 0.12 (BF60) and 0.3 (BF40). Thus, for the lower magnetic field configuration, I_{prim} represents a larger contribution to the discharge current compared with the other magnetic field case. Despite this, both HiPIMS discharges have entered the recycling regime, which is not surprising since the measured discharge currents are well above I_{crit}. To establish whether the discharge is dominated by self-sputtering recycling or gas recycling, I_{SS} and $I_{gas-recycle}$ must be compared to I_D. For BF60 and BF40 configurations, I_{SS}/I_D and $I_{gas-recycle}/I_D$ are approximately equal to 0.86 and 0.02 and to 0.66 and 0.04, respectively. For greater clarity, Fig. 9 exhibits the so-called recycling map [34], which allows to represent a discharge by a point as a function of the associated $I_{gas-recycle}/I_D$ and I_{SS}/I_D values. Specifically, the red-colored region identifies DCMS-like discharges, while the blue-colored region discharges dominated by recycling (A: self-sputtering recycle range, B: gas-recycle range, AB: mixed-recycling range).

Fig. 9 highlights how, for both *B-fields*, gas recycling plays a minor role in agreement with the Ar^+ ion contribution to the discharge currents (see Fig. 1(b) and 1(c)). On the other hand, self-sputtering recycling is the most important process in the two discharges. However, this recycling mechanism has a distinct impact in the two cases. Indeed, if the magnetic field is increased by fixing other process parameters, a larger current is obtained. As a consequence, to sustain the discharge, a larger number of sputtered metal atoms must be ionized and, successively, back-attracted to the target resulting in an increment of self-sputtering recycling. This explains the higher values of β and $F_{Dens,W}$ (see Fig. 2 (e)) found for the BF60 configuration than for the BF40 one. In Fig. 9, this results in a shift along the y-axis as magnetic field is increased from 40 to 60 mT. Moreover, the points representing the discharges analyzed by *Babu et al.* [47] are plotted in Fig. 9 showing that, for the Ar/W system, a similar effect is obtained increasing the discharge voltage. It is worth to mention that, despite the different experimental conditions, the general behavior of plasma parameters retrieved from our modeling and the fitting parameter values are in reasonable agreement with the findings of [47]. Thus, the adopted modeling approach allowed to investigate the impact of *B-field* on the main physical mechanisms governing the Ar/W HiPIMS plasma and, exploiting the general concepts of $I_{gas-recycle}/I_D$ and I_{SS}/I_D, to perform interesting comparisons between different discharges. Specifically, since a *B-field* increase results in a stronger ionization and an enhanced back-attraction, a careful choice of the magnetic field strength should be carried out to find the optimum condition both in terms of film properties and deposition rate [48].

In addition to the magnetic field strength, we considered the role of a high pulsed bias voltage, both synchronized and delayed to the voltage pulse onset. Since bias directly influences the ionized species impinging on the substrate, it is worth having at least a qualitative picture of the behavior of the ionized flux originating from IR. From Fig. 2(f), the temporal evolution of $F_{Flux,W}$ can be appreciated. During the voltage pulse on-time, despite the larger $F_{Dens,W}$ observed for BF60 configuration (Fig. 2(e)), $F_{Flux,W}$ is nearly equal (10–15 %) for both *B-field* conditions. This is due to the enhanced ion back-attraction for the higher magnetic field configuration. However, during the afterglow, $F_{Flux,W}$ becomes strongly different. When the voltage pulse is switched off, the back-attraction probability goes to zero and, ideally, all the sputtered ions are free to move towards the growing films. Thus, $F_{Flux,W}$ experiences an instantaneous increase which depends on the $F_{Dens,W}$ value characterizing the plasma. Roughly, $F_{Flux,W}$ increases up to 20 % in the BF40 configuration and up to 40 % in the BF60 one.

An approximated estimation of the ion flux composition at IR borders, extracted from modeling results, is reported for BF40 and BF60 configurations in Fig. 10(a) and (b), respectively. In both cases, during the voltage pulse, the ion flux composition reflects the temporal evolution of the discharge current composition. Except for the ignition phase, the ion flux is dominated by W^+ ions at different extent according to the *B-field* condition examined. For the BF60 configuration, the situation is similar also during the afterglow. After about 90 μs from the voltage pulse end, a switch between Ar^+ and W^+ ions is observed. On the contrary, for BF40 configuration, W^+ ions dominate in the afterglow only for approximately 30 μs. Successively, Ar^+ ions represent the main species in the ion flux composition. Thus, among the two *B-field* configurations, the action of Ar^+ ions should be more relevant for the BF40 condition since, during both pulse on-time and afterglow, their contribution to the ion flux originating from IR is larger with respect to the BF60 case. It is worth noticing that, since back-attraction becomes null when the pulse is switched off, the ion flux value experiences an increase at afterglow beginning, independently on magnetic field configuration. The presented qualitative picture allows us to carry out some considerations about the experimental results reported in Section 3.2. It must be noted that in the following analysis, although worthy of consideration, the transport process of ionized species towards the substrate is not included since it is beyond the aim of the modeling work presented.

The adatoms mobility on the growing film surface is one of the major factors influencing polycrystalline films growth evolution. Generally, mobility is determined by the homologous temperature $T_h = T_s/T_m$ (i.e., the ratio between substrate temperature and melting temperature of the deposited material). If $T_h < 0.2$, adatoms are characterized by a limited mobility leading to the generation of tensile stress [78]. However, if an energetic deposition technique such as HIPIMS is considered, a compressive stress state can be observed. As reported in the literature [78,79], the implantation of bombarding gas ion species or the formation of point defects are usually indicated as the main processes triggering the compressive stress state. Specifically, these mechanisms cause a hydrostatic (triaxial) expansion of the crystal lattice. Thus, a significant hydrostatic component characterizing the stress state results in a stress-free lattice parameter substantially larger than the unstrained value. On the other hand, other mechanisms can take place. As stated by *Magnfält et al.* [79], the migration of the adatoms to the under-dense grain boundaries can happen also for $T_h < 0.2$ if a large flux of species with energies in the hyperthermal range (10s–100s eV) is present during film growth. Differently from the previous mechanisms, this process promotes a biaxial stress component rather than a hydrostatic component. As a result, in such a condition, the stress-free lattice parameter is slightly affected by the stress state and its expansion is small. For example, considering molybdenum films produced by different

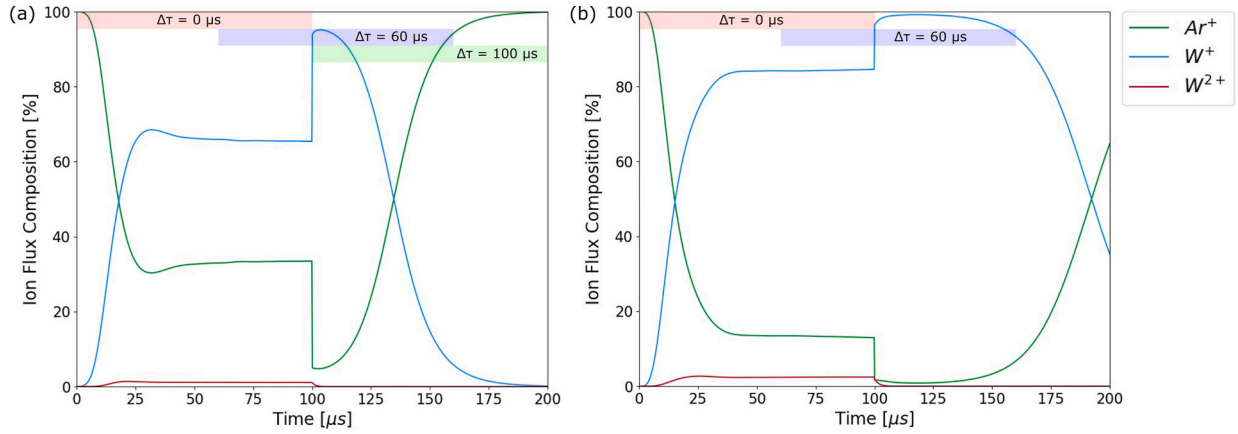

Fig. 10. Ion flux composition at IR borders extracted from IRM for (a) BF40 and (b) BF60 configurations. The temporal intervals during which the pulsed bias was applied are indicated. The legend on the right refers to both (a) and (b) panels.

sputtering techniques [79–81], the crystallite group and the $sin^2\psi$ methods [79] were exploited to retrieve stress-free lattice parameter and, in turn, the main stress component in the films. Differently, the out-of-plane lattice parameter value is influenced by both biaxial and hydrostatic components, thus not allowing to attribute the compressive stress to a specific mechanism. Despite this, at preliminary level, its percentage change with respect to the unstrained bulk value can be indicative of a variation of films growth conditions [82–85].

In the present study, T_h is well-below 0.2. Indeed, no intentional heating was applied to the substrate and, also considering a growth temperature increase caused by the high ion energy examined, the variation on T_h value can be considered small due to the high melting point of W (~3400 °C). As reported in Sections 3.2.1 and 3.2.3, all produced films are characterized by an out-of-plane lattice parameter expansion and thus a compressive stress state. In light of the above considerations, this can be ascribed to the hyperthermal ion flux characterizing the investigated Ar/W HiPIMS discharge. In this regard, the ion flux characteristics, influenced by both magnetic field strength and substrate bias configuration, are crucial in determining the specific film growth process and, in turn, its properties.

The value $U_S = 200$ V has been examined for BF40 configuration only since, for the BF60 case, this accelerating voltage was not sufficient for films adhesion. Under this condition, independently on the ion flux composition accelerated towards the substrate (i.e., the bias delay), the deposited films exhibit similar properties. All samples are characterized by a densely packed columnar structure associated with a preferential ⟨110⟩-orientation of the α-W phase and by comparable values of mass thickness, density and composition. Moreover, the shift of the α-{110} peak position in the acquired X-ray diffractograms indicates the presence of residual compressive stresses which is confirmed by substrate curvature measurements.

As depicted in Fig. 3(c), the out-of-plane lattice parameter variation is always in the range 0.4–0.6 %. Considering these percentage variations and the U_S value applied, a hydrostatic strain field is probably the mechanism triggering the stress. It is interesting to note that XRD and stress analyses are in reasonable agreement with the findings of *Shimizu et al.* [38], where W films were grown in presence of a pulsed bias voltage. Probably, in this ion energy range an analogous behavior can be assumed also for the BF60 configuration. As shown in Fig. 5(a), a bias voltage value of 200 V determines a morphology similar to the BF40 one, along with even larger internal stresses, which can explain films failure in this deposition condition.

Concerning the highest bias amplitude, $U_S = 800$ V, film properties show a more pronounced dependence on the accelerated ion flux composition (i.e., different magnetic field strength and bias delay). For both magnetic field configurations, the α-W ⟨110⟩-orientation remains the main one, but films show a transition to a larger column size structure with more uniform surface. This behavior agrees with the structure zone diagram (SZD) for energetic depositions proposed by *Anders* [86] in which a preferred orientation and larger size columnar grains are foreseen when the energy of bombarding particles is increased. Despite this, the evolution of density and Ar content shows a different behavior varying the magnetic field strength. In both configurations, if $\Delta\tau = 0$ μs, density is near the bulk one and the Ar content around 1 %. This can be ascribed to the limited ion action due to back-attraction to the target. By delaying the bias pulse, the lower *B-field* condition leads to a significant density reduction and to a larger concentration of Ar impurities. On the other hand, if the bias pulse is delayed in the higher *B-field* condition, density slightly decreases, and the Ar content increase is less pronounced. A possible explanation can be hypothesized by examining films stress state. In the two cases, substrate curvature measurements reveal the presence of a compressive stress state which, on average, results larger in the BF60 condition. However, with respect to $U_S = 200$ V, the out-of-plane lattice parameter variation reduces to values around 0.22–0.25 % suggesting that compressive stress may be triggered by different mechanisms. Likely, in addition to implantation and point defects formation, atom insertion into grain boundaries may be promoted due to the remarkably high energy of the impinging ionized hyperthermal flux. Particularly, according to the specific ionized species bombarding the growing films, different effects are generated. In the BF60 configuration, since the ionized flux originating from IR is always dominated by W^+ species (see Fig. 10(b)), it can be expected that ion species accelerated towards the substrate by the applied bias voltage will be mostly W^+ ones. Therefore, the diffusion of W atoms towards under-dense regions plays an important role. This results in grain boundaries densification which, in turn, leads to the reported density and Ar content trends. Differently, in the BF40 configuration, the ionized flux originating from IR exhibits a larger Ar^+ ion contribution (see Fig. 10(a)) implying that, besides W^+ species, a not negligible amount of Ar^+ ions impinge on the growing films. Therefore, compressive stress generation is triggered by diffusion towards grain boundaries of both W and Ar atoms. Specifically, this could clarify the density reduction and the Ar content increase since Ar atoms remain trapped at grain boundaries. Moreover, for this energy range, the previously mentioned SZD foresees a substantial re-sputtering. As visible in Figs. 4–6, this effect is strongly dependent on bias voltage delay. When the accelerating bias is synchronous with the voltage pulse, mass thickness shows a moderate decrease in the two magnetic field conditions since back-attraction limits ion action at substrate. On the contrary, the situation is strongly different when the bias voltage application is temporarily delayed. For the BF60 case, the combination between the high energy range considered and the W^+ dominated ion

flux determines a huge films re-sputtering which results in the net deposition of only the 20 % of the material. In this respect, SRIM simulations [87] suggest only a marginal role of W^+ ion backscattering. For the BF40 case, an increase of re-sputtering is visible even if at lower extent compared to the previous magnetic strength condition probably due to the higher fraction of Ar^+ species in the ion flux.

Moving to the intermediate bias amplitude investigated, $U_S = 400$ V, all films exhibit similar morphology and a preferred α-W ⟨110⟩-orientation as in the previous cases. However, out-of-plane lattice parameter variation may indicate that different mechanisms cause the generation of compressive stress observed in films deposited under BF40 or BF60 configuration. In the latter case, since a variation of about 0.22–0.25 % is observed, compressive stresses could be considered biaxial and promoted by atom insertion into grain boundaries. Therefore, the same considerations expressed for the $U_S = 800$ V condition should apply to this energy range but considering a lower penetration depth for impinging ions. Indeed, films density approaches the bulk one and the Ar content is low. Moreover, if the bias is delayed, a significant re-sputtering effect is observed although limited with respect to the previous case. Regarding the BF40 configuration, the out-of-plane lattice parameter variation is always larger than 0.3 %, suggesting that the main mechanism triggering the stress state are probably similar to the ones observed in the $U_S = 200$ V condition. This, in addition to the possibility of annihilating the previously mentioned defects during deposition by other ions, could justify the differences in Ar content and density observed with respect to the $U_S = 800$ V condition. For this intermediate case, it is worth highlighting the significant role of magnetic field strength. Indeed, under the same bias conditions, different processes take place at growing film surface according to the specific ion flux composition impinging at substrate which, in turn, is determined by the *B-field* configuration. However, for an exhaustive comprehension of film properties, other factors should be considered. For example, as mentioned before, a proper study of the particle transport process by means of both experimental and computational tools would allow retrieving more accurate information about the ion flux at the substrate. Furthermore, the role of back-scattered working gas atoms from the cathode could be relevant for W film growth, as already observed during the sputtering of other high-Z elements [88,89].

In summary, the specific ion flux behavior characterizing the analyzed deposition conditions, highlighted by modeling analysis, induced different processes at film surface during its growth. As a result, W films exhibiting different properties have been obtained, potentially attractive for specific application. Referring to PWI research area, considering both *B-field* examined, films deposited with a synchronized bias pulse ($\Delta\tau = 0$ μs, $U_S = 400$, 800 V) could be suitable to be exploited in erosion or corrosion experiments [16,22,90] due to their near bulk density and compact superficial morphology. On the other hand, films grown with the lower magnetic field strength and large, delayed bias pulse ($U_S = 800$ V, $\Delta\tau = 60$, 100 μs) could be of interest to study W gas retention mechanisms [17,91] since, in these conditions, a significant fraction of working gas remains trapped during the deposition. Furthermore, it is notable that the HiPIMS bias conditions examined could be compatible with experiments aimed to better understand the behavior of W in a fusion-relevant environment [90,92]. Thus, HiPIMS plasma could be used as a tool for PWI studies, as already done in DCMS regime [93].

5. Conclusions

The HiPIMS Ar/W system has been investigated by a combined modeling and experimental approach to explore its complex physics. In the modeling analysis, we examined the influence of two magnetic field strengths (40 and 60 mT) on plasma conditions. Model results showed that to a variation of magnetic field strength corresponded a different self-sputtering recycling degree, which was stronger for the higher case. The amplification of this mechanism influenced, in turn, the sputtered ion fraction in the plasma and the ion back-attraction towards the target. For this reason, despite a higher $F_{Dens,W}$ in the 60 mT case, $F_{Flux,W}$ was nearly equal in the two magnetic field configurations during the on-time of the voltage pulse. On the other hand, since back-attraction ion probability is zero in the afterglow, the previously mentioned ratio and the ion flux composition became dramatically different in the two conditions. This is relevant for process reproducibility since, due to target erosion during HiPIMS operations, a magnetic field strengthening occurs.

We exploited the examined discharges to deposit films in presence of a negative pulsed bias voltage, both synchronized and delayed to the voltage pulse onset. Morphology, microstructure, stress state, composition and density of the produced films have been studied. In this respect, microstructure and stress measurements suggested that different phenomena took place during films deposition according to the magnetic field strength and bias configuration considered. Thus, the analysis highlighted how the choice of specific process parameters results crucial in determining the ion flux composition accelerated towards the substrate and, in turn, the mechanisms taking place at growing film surface. To conclude, the reported combined approach allowed to achieve a satisfactory understanding of the connection between the characteristics of the HiPIMS Ar/W discharge and the experimentally observed properties of the deposited films as process parameters are varied. Thus, the presented results could be of interest for the production of properly tailored W and W-based films in different applicative sectors. With particular reference to magnetic confinement fusion research, the HiPIMS W plasma could be suitable both for the realization of fusion-relevant coatings and as environment for PWI studies.

CRediT authorship contribution statement

D. Vavassori: Writing – original draft, Writing – review & editing, Conceptualization, Investigation, Formal analysis, Visualization. **F. Mirani:** Writing – review & editing, Formal analysis, Visualization. **F. Gatti:** Formal analysis, Writing – review & editing. **D. Dellasega:** Conceptualization, Formal analysis, Supervision, Writing – review & editing. **M. Passoni:** Supervision, Funding acquisition, Writing – review & editing.

Declaration of competing interest

The authors declare that they have no known competing financial interests or personal relationships that could have appeared to influence the work reported in this paper.

Data availability

The data supporting the findings of this work are available from the corresponding authors upon reasonable request.

Acknowledgements

This work has been partially carried out within the framework of the EUROfusion Consortium, funded by the European Union via the Euratom Research and Training Programme (Grant Agreement No 101052200 — EUROfusion). Views and opinions expressed are however those of the author(s) only and do not necessarily reflect those of the European Union or the European Commission. Neither the European Union nor the European Commission can be held responsible for them.

Appendix A. Model geometry and equations

In this Appendix, the geometry of IR and the equations used in the model for the different populations are reported.

A.1. Ionization Region geometry

The IR volume is an annular cylinder with a rectangular section. The inner radius ($r_{c,1}$) and the outer radius ($r_{c,2}$) are estimated from the area of the race-track region and light emission. The height L is calculated as the difference between the axial extension of IR into the chamber (z_2) and the sheath thickness between the plasma and the sputtered target (z_1). Specifically, as reported by *Zanáška et al.* [94], z_2 is approximated by the distance of the magnetic null point from the target. Instead, z_1 is determined using the Child sheath law as generally assumed in the literature [44]. For both BF40 and BF60 configurations, $r_{c,1}$ and $r_{c,2}$ are set equal to 1.5 cm and 2.9 cm, respectively. Instead, z_1 and z_2 values are set to 0.3 cm and 1.3 cm in the BF40 case and 0.1 cm and 1.6 cm in the BF60 case.

A.2. Atoms and ions balance equations

The model was implemented in *Python*, and the equations were solved through the *solve_ivp* function contained in the *SciPy* package [95]. For each reaction, the rate coefficients are listed in Table 2. The symbols of the parameters appearing in the equations are resumed in Table B1.

Table B1
Parameters of the Ar/W system IRM.

Symbol	Description	Unit
e	Elementary Charge Constant	[C]
f	$f = U_{IR}/U_D$ (fit parameter)	
F_{coll}	Collision probability Ar-W	[Hz]
k_b	Boltzmann constant	[J/K]
k	Rate coefficient	[m^3/s]
I_D	Experimental discharge current	[A]
I_{calc}	Simulated discharge current	[A]
I_{SE}	Secondary electron current	[A]
L	Length of the IR	[m]
m	Particle mass	[kg]
n	Particle density	[m^{-3}]
P	Argon pressure [Pa]	
r	Secondary electron recapture probability	
r_X	Particle radius	[m]
S_{IR}	Area of Ionization Region	[m^2]
S_{RT}	Area of Ionization Region towards the race-track	[m^2]
t	Time	[s]
T_e	Cold electron temperature	[eV]
T_eH	Hot electron temperature	[eV]
T_X	Average particle energy	[eV]
U_D	Experimental discharge voltage	[V]
U_{IR}	Voltage across the Ionization Region	[V]
U_{SH}	Sheath voltage $U_{SH} = U_D - U_{IR}$	[V]
V_{IR}	Volume of the Ionization Region	[m^3]
Y	Sputtering yield	
β	Back-attraction probability (fit parameter)	
ϵ_0	Dielectric constant	[F/m]
σ	Collision cross section	[m^2]
Γ	Particle flux	[1/(m^2·s)]
γ	Secondary electron emission coefficient	

A.2.1. Cold argon atoms

$$\frac{dn_{Ar}}{dt} = \left(-k^C_{iz,Ar}n_{e^C} - k^C_{ex,Ar}n_{e^C} - k^H_{iz,Ar}n_{e^H} - k^H_{ex,Ar}n_{e^H}\right)n_{Ar} + \left(k^C_{dex,Ar^m}n_{e^C} + k^H_{dex,Ar^m}n_{e^H}\right)n_{Ar^m} + k_{chexc}n_W n_{Ar^+} - k_{chexc,2}n_{Ar}n_{W^{2+}} + k_P n_{Ar^m}n_W + \frac{\Gamma_{Ar,diff}\cdot(S_{IR}-S_{RT})}{V_{IR}} - \frac{\left(\Gamma_{W,0}+\Gamma_{W^+,0}+\Gamma_{W^{2+},0}\right)F_{coll}(S_{IR}-S_{RT})}{V_{IR}}\cdot\frac{m_W}{m_{Ar}}\cdot\frac{n_{Ar}}{n_{Ar}+n_{Ar^m}} \quad \text{(A1)}$$

$\Gamma_{Ar,\,diff} = [(n_{Ar,\,0} - n_{Ar})u_{Ar}]/2$ represents the diffusional Ar flux where $n_{Ar,\,0}$ is the Ar density outside the IR calculated with the ideal gas law, and u_{Ar} is the random thermal velocity defined as $u_{Ar} = \sqrt{(2eT_{Ar})/\pi m_{Ar}}$ with $T_{Ar} = 0.026$ eV (300 K). The last term in Eq. (A1) takes into account the sputtering wind effect, where $\Gamma_{M,0} = (n_M u_M)/2$ (M=W,W^+,W^{2+}) is the sputtering wind flux of W species, and $u_M = \sqrt{(3k_bT_M)/m_M}$ is their root mean square velocity. The average energy of sputtered species is defined in Section 3.1. F_{coll} is the collision probability of W particles with the working gas particles in the IR defined as

$$F_{coll} = 1 - exp[\sigma_{Ar-W}L(n_{Ar} + n_{Ar^H} + n_{Ar^W} + n_{Ar^m})] \quad \text{(A2)}$$

In Eq. (A2), $\sigma_{Ar-W} = \pi(r_W + r_{Ar})^2$ is estimated using the hard sphere model cross section with $r_W = 1.41 \times 10^{-10}$ m and $r_{Ar} = 1.88 \times 10^{-10}$ m [96].

A.2.2. Hot argon atoms

$$\frac{dn_{Ar^H}}{dt} = -\frac{\Gamma_{Ar^H,diff}}{L} + \xi_{pulse}\xi_H \Gamma^{RT}_{Ar^+}\frac{S_{RT}}{V_{IR}} + \left(-k^C_{iz,Ar}n_{e^C} - k^C_{ex,Ar}n_{e^C} - k^H_{iz,Ar}n_{e^H} - k^H_{ex,Ar}n_{e^H}\right)n_{Ar^H} \tag{A3}$$

Ar^H atoms are the argon ions that, after bombarding the target, immediately return to the IR as neutrals with the energy of few eV. ξ_{pulse} is the fraction of argon ions which return to the IR during the pulse, while ξ_H is the fraction assumed to return as hot argon ions. Here, ξ_{pulse} is set equal to 1 and ξ_H to 0.5. More details about these two parameters can be found in [44]. Specifically, the diffusion flux is given by $\Gamma_{Ar^H,\,diff} = n_{Ar^H}u_{Ar^H}$, where u_{Ar^H} is the random thermal velocity with $T_{Ar^H} = 2$ eV. The ion flux towards the race-track Γ^{RT}_i (i= Ar^+ in Eq. (A3)) depends on the fitting parameter β and is taken as defined in [35].

A.2.3. Warm argon atoms

$$\frac{dn_{Ar^W}}{dt} = -\frac{\Gamma_{Ar^W,diff}}{L} + \xi_{pulse}(1-\xi_H)\Gamma^{RT}_{Ar^+}\frac{S_{RT}}{V_{IR}} + \left(-k^C_{iz,Ar}n_{e^C} - k^C_{ex,Ar}n_{e^C} - k^H_{iz,Ar}n_{e^H} - k^H_{ex,Ar}n_{e^H}\right)n_{Ar^W} \tag{A4}$$

Ar^W atoms are the argon ions that, when bombarding the target, penetrate its surface and then, once neutralized, come back in the IR [44]. The diffusion flux is defined as in Eq. (A3), but assuming $T_{Ar^W} = 0.1$ eV.

A.2.4. Metastable argon atoms

$$\begin{aligned}\frac{dn_{Ar^m}}{dt} &= \left(-k^C_{iz,Ar^m}n_{e^C} - k^H_{iz,Ar^m}n_{e^H}\right)n_{Ar^m} + \left(-k^C_{dex,Ar^m}n_{e^C} - k^H_{dex,Ar^m}n_{e^H}\right)n_{Ar^m} + \left(k^C_{ex,Ar}n_{e^C} + k^H_{ex,Ar}n_{e^H}\right)(n_{Ar} + n_{Ar^H} + n_{Ar^W}) - k_P n_{Ar^m}n_W - \frac{\Gamma_{Ar^m,diff}\cdot(S_{IR}-S_{RT})}{V_{IR}} \\ &\quad - \frac{(\Gamma_{W,0} + \Gamma_{W^+,0} + \Gamma_{W^{2+},0})F_{coll}(S_{IR}-S_{RT})}{V_{IR}}\cdot\frac{m_W}{m_{Ar}}\cdot\frac{n_{Ar^m}}{n_{Ar}+n_{Ar^m}}\end{aligned} \tag{A5}$$

The diffusion flux for Ar^m species is defined as $\Gamma_{Ar^m,diff} = (n_{Ar^m}u_{Ar^m})/2$, where u_{Ar^m} is their random thermal velocity calculated assuming $T_{Ar^m} = 0.1$ eV [97].

A.2.5. Argon ions

$$\frac{dn_{Ar^+}}{dt} = \left[k^C_{iz,Ar}(n_{Ar}+n_{Ar^H}+n_{Ar^W}) + k^C_{iz,Ar^m}n_{Ar^m}\right]n_{e^C} + \left[k^H_{iz,Ar}(n_{Ar}+n_{Ar^H}+n_{Ar^W}) + k^H_{iz,Ar^m}n_{Ar^m}\right]n_{e^H} - k_{chexc}n_W n_{Ar^+} + k_{chexc,2}n_{W^{2+}}n_{Ar} - \frac{\left[\Gamma^{RT}_{Ar^+}S_{RT} + (S_{IR}-S_{RT})\Gamma^{BP}_{Ar^+}\right]}{V_{IR}} \tag{A6}$$

Γ^{BP}_i (i = Ar^+ in Eq. (A6)) represents the ion flux outside the IR towards the diffusion region (i.e., the chamber/substrate). It depends on the fitting parameter β, as defined in [35].

A.2.6. Tungsten atoms

$$\frac{dn_W}{dt} = -k^C_{iz,W}n_W n_{e^C} - k^H_{iz,W}n_W n_{W^+}n_{e^H} - k_P n_W n_{Ar^m} - k_{chexc}n_W n_{Ar^+} + \frac{\left(\Gamma^{RT}_{Ar^+}Y_{Ar^+} + \Gamma^{RT}_{W^+}Y_{W^+}\Gamma^{RT}_{W^{2+}}Y_{W^{2+}}\right)S_{RT}}{V_{IR}} - \frac{\Gamma_{W,diff}\cdot(S_{IR}-S_{RT})}{V_{IR}} \tag{A7}$$

The fourth term in Eq. (A7) represents W atoms production from the target bombardment due to the different ionized species considered in the model. Specifically, Y_{Ar^+}, Y_{W^+} are the sputter and self-sputter yields as defined in Section 2.1.2, setting $E_i = U_D$, while $Y_{W^{2+}}$ is calculated setting $E_i = 2U_D$. The diffusion flux of W atoms is defined as $\Gamma_{W,\,diff} = \Gamma_{W,\,0}(1 - F_{coll})$.

A.2.7. Singly charged W ions

$$\frac{dn_{W^+}}{dt} = k^C_{iz,W}n_W n_{e^C} + k^H_{iz,W}n_W n_{e^H} + k_P n_W n_{Ar^m} + k_{chexc}n_W n_{Ar^+} + k_{chexc,2}n_{W^{2+}}n_{Ar} - k^C_{iz,W^+}n_{W^+}n_{e^C} - k^H_{iz,W}n_{W^+}n_{W^+}n_{e^H} - \frac{\Gamma^{RT}_{W^+}S_{RT} + \Gamma^{BP}_{W^+}(S_{IR}-S_{RT})}{V_{IR}} \tag{A8}$$

A.2.8. Doubly charged W ions

$$\frac{dn_{W^{2+}}}{dt} = k^C_{iz,W^+}n_{W^+}n_{e^C} + k^H_{iz,W^+}n_{W^+}n_{e^H} - k_{chexc,2}n_{W^{2+}}n_{Ar} - \frac{\Gamma^{RT}_{W^{2+}}S_{RT} + \Gamma^{BP}_{W^{2+}}(S_{IR}-S_{RT})}{V_{IR}} \tag{A9}$$

A.3. Electrons balance equations

A.3.1. Cold electrons

$$n_{e^C} = n_{Ar^+} + n_{W^+} + 2n_{W^{2+}} - n_{e^H} \tag{A10}$$

The density of cold electrons is calculated assuming that the quasi-neutrality approximation holds for the HiPIMS discharge.

A.3.2. Hot electrons

$$\frac{dn_{e^H}}{dt} = \frac{1}{0.5 \cdot U_D}\left[\frac{U_{SH}}{eV_{IR}} I_{SE} - \left(E_{Ar,c,eff} + E_{htc}\right)k^H_{iz,Ar} n_{e^H}\left(n_{Ar} + n_{Ar^H} + n_{Ar^W}\right) - \left(E_{Ar^m,c,eff} + E_{htc}\right)k^H_{iz,Ar^m} n_{e^H} n_{Ar^m} - \left(E_{W,c,eff} + E_{htc}\right)k^H_{iz,W} n_{e^H} n_W - \left(E_{W^+,c,eff} + E_{htc}\right)k^H_{iz,W^+} n_{e^H} n_{W^+} + E_{dex,Ar^m} k^H_{dex,Ar^m} n_{e^H} n_{Ar^m}\right] \tag{A11}$$

In the first term inside square brackets, U_{SH} is the sheath potential defined in Table 2 while I_{SE} is the secondary electron current defined as $I_{SE} = \gamma_{Ar^+,\,eff} \Gamma^{RT}_{Ar^+} + 0.5\,\gamma_{W^{2+},\,eff} \Gamma^{RT}_{W^{2+}}$.

$E_{c,\,eff}$ represents the loss of energy per ion-electron pair created, which for the $i-th$ species (i = Ar, Ar^m, W and W^+ in Eq. (A11)) is equal to:

$$E_{i,c,eff} = E_{i,iz} + E_{i,ex}\frac{k_{i,ex}}{k_{i,iz}} + \frac{k_{i,el}}{k_{i,iz}}\frac{3m_e}{m_i}T_e \tag{A12}$$

Specifically, the second term in Eq. (A12) is not considered for Ar^m and W^+ species. E_{htc}, the average energy released to the cold electrons when a hot electron causes ionization, is set equal to 10 eV [44].

A.4. Cold electron temperature equation

$$\frac{2}{3} n_{e^C}\frac{dT_e}{dt} = E_{htc}\nu^H_{iz} + \frac{1}{2} f \frac{I_D U_D}{eV_{IR}} + E_{dex,Ar^m} k^C_{dex,Ar^m} n_{e^C} n_{Ar^m} \frac{1}{2} T_e \frac{\left[\left(\Gamma^{RT}_{Ar^+} + \Gamma^{RT}_{W^+} + \Gamma^{RT}_{W^+}\right)S_{RT} + \left(\Gamma^{BP}_{Ar^+} + \Gamma^{BP}_{W^+} + \Gamma^{BP}_{W^+}\right)\left(S_{IR} - S_{RT}\right)\right]}{V_{IR}} - \left(E_{Ar,c,eff} + \frac{3}{2}T_e\right) n_{e^C}\left(n_{Ar} + n_{Ar^H} + n_{Ar^W}\right) - \left(E_{Ar^m,c,eff} + \frac{3}{2}T_e\right) n_{e^C} n_{Ar^m} \left(E_{W,c,eff} + \frac{3}{2}T_e\right) n_{e^C} n_W - \left(E_{W^+,c,eff} + \frac{3}{2}T_e\right) n_{e^C} n_{W^+} \tag{A13}$$

In the first term, on the right-hand side of Eq. (A13), the quantity ν^H_{iz} accounts for the ionization frequency of the hot electron population. It is given by:

$$\nu^H_{iz} = n_{e^H}\left[k^H_{iz,Ar}\left(n_{Ar} + n_{Ar^H} + n_{Ar^W}\right) + k^H_{iz,Ar^m} n_{Ar^m} + k^H_{iz,W} n_W + k^H_{iz,W^+} n_{W^+}\right] \tag{A14}$$

In the second term on the right-hand side of Eq. (A13), f is the other fitting parameter of the model and represents the fraction of the discharge voltage falling over the IR.

Appendix B. Magnetic field simulation

The 3D static magnetic field associated with the magnetron sputter source was retrieved with the Finite Element Method (FEM). We implemented the geometry reported in Fig. B1(a) in the Gmsh finite element mash generator [98]. It consists of a central conical pole surrounded by eighteen rectangular magnets. A copper plate, whose function is to support the sputtering target, is located 5 mm above the external ring. We neglect the presence of the target in the simulation geometry since tungsten is a paramagnetic material with relative permeability close to unity. All the elements are located in a simulation box of 150 × 150 × 120 mm. The mesh (i.e., ~10^4 nodes, 1.5 × 10^5 edges and 5 × 10^5 faces) is imported in a magnetostatic FEM code based on the Sparselizard c++ library [99]. A 2D magnetostatic example is provided along with the Sparselizard source code. We refer to this example for a detailed description of the electrostatic problem and its implementation. For the magnets (i.e., NdFeB type with grade N35) and copper, we assume a relative permeability of 1.05 and 1.002, respectively. The magnet residual magnetic flux density (i.e., remanence) is $B_r = 1.25$ T.

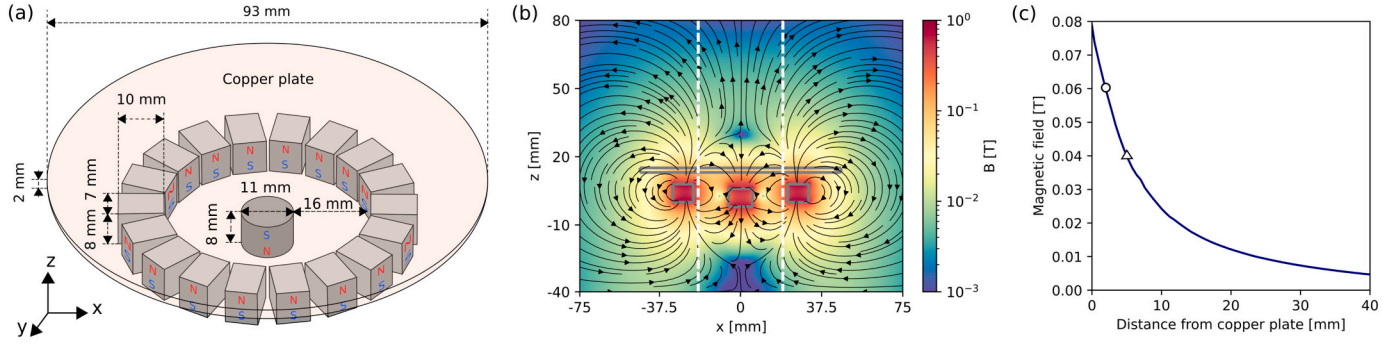

Fig. B1. (a) The magnetron simulation geometry. (b) The magnetic field distribution in the x-z plane, crossing the middle of the central dipole. The dashed lines indicate the target race-track mid-point. (c) The magnetic field strength as a function of distance from the copper plate surface and for $x \sim 20$ mm. The circle refers to the BF60 configuration, while the triangle to the BF40 one.

The resulting magnetic field intensity distribution in the x-z plane perpendicular to the copper plate is depicted in Fig. B1(b). The null point is located ~17 mm above the copper surface. The mid-point of the race-track, located approximately at x ~ ±20 mm in the considered plane, is highlighted by dashed white lines in Fig.B1(b). At this radial position, Fig. B1(c) shows the magnetic field strength evaluated as a function of the distance from the copper plate. The azimuthal position corresponding to the race-track surface of the thin and thick W targets are indicated with a circle (~2 mm) and a triangle (~5 mm), respectively. The magnetic field strength rapidly vanishes within few cm distance from the target support surface.

References

[1] G. Chen, L. Yang, H. Tian, C. Hsu, Evaluating substrate bias on the phase-forming behavior of tungsten thin films deposited by diode and ionized magnetron sputtering, Thin Solid Films 484 (1) (2005) 83–89, https://doi.org/10.1016/j.tsf.2005.02.032, issn: 0040-6090.

[2] P. Zheng, B.D. Ozsdolay, D. Gall, Epitaxial growth of tungsten layers on mgo(001), J. Vac. Sci. Technol. A 33 (6) (2015) 061–505, https://doi.org/10.1116/1.4928409.

[3] N. Radić, A. Tonejc, J. Ivkov, P. Dubček, S. Bernstorff, Z. Medunić, Sputter-deposited amorphous-like tungsten, Surf. Coat. Technol. 180-181 (2004) 66–70, https://doi.org/10.1016/j.surfcoat.2003.10.038, issn: 0257-8972.

[4] M. Spindler, et al., Chemical etching of tungsten thin films for high-temperature surface acoustic wave-based sensor devices, Thin Solid Films 612 (2016) 322–326, https://doi.org/10.1016/j.tsf.2016.04.035, issn: 0040- 6090.

[5] G. Vijaya, M.M. Singh, M. Krupashankara, M. Srinivas, R. Kulkarni, Development and analysis of tungsten thin film coating for solar absorption, Mater.TodayProc. 5 (1, Part 3) (2018) 2555–2563, https://doi.org/10.1016/j.matpr.2017.11.039.

[6] K. Sibin, S. John, H.C. Barshilia, Control of thermal emittance of stainless steel using sputtered tungsten thin films for solar thermal power applications, Sol. Energy Mater. Sol. Cells 133 (2015) 1–7, https://doi.org/10.1016/j.solmat.2014.11.002, issn: 0927-0248.

[7] C. Ruset, et al., Development of w coatings for fusion applications, no. 9, in: Fusion Engineering and Design, Proceedings of the 26th Symposium of Fusion Technology (SOFT-26), vol. 86, 2011, pp. 1677–1680, https://doi.org/10.1016/j.fusengdes.2011.04.031.

[8] D. Dellasega, G. Merlo, C. Conti, C.E. Bottani, M. Passoni, Nanostructured and amorphous-like tungsten films grown by pulsed laser deposition, J. Appl. Phys. 112 (8) (2012) 084–328, https://doi.org/10.1063/1.4761842.

[9] S. Brezinsek, et al., Plasma–wall interaction studies within the eurofusion consortium: progress on plasma-facing components development and qualification, Nucl.Fusion 57 (11) (2017), https://doi.org/10.1088/1741-4326/aa796e, pp. 116 041.

[10] F. Romanelli, L. Federici, R. Neu, D. Stork, H. Zohm, A roadmap to the realization of fusion energy, in: Proc. IEEE 25th Symp. Fusion Eng, 2013, pp. 1–4, issn: 0927-0248.

[11] R. Pitts, et al., Physics basis for the first iter tungsten divertor, Nucl.Mater.Energy 20 (2019) 100–696, https://doi.org/10.1016/j.nme.2019.100696.

[12] R.L. Neu, et al., Experiences with tungsten plasma facing components in asdex upgrade and jet, IEEE Trans.Plasma Sci. 42 (3) (2014) 552–562, https://doi.org/10.1109/TPS.2014.2298253.

[13] M. Firdaouss, et al., Overview of the different processes of tungsten coating implemented into west tokamak, in: Fusion Engineering and Design, Proceedings of the 29th Symposium on Fusion Technology (SOFT-29) Prague, Czech Republic, September 5-9, 2016, vol. 124, 2017, pp. 207–210, https://doi.org/10.1016/j.fusengdes.2017.02.087, issn: 0920-3796.

[14] M. 't Hoen, D. Dellasega, A. Pezzoli, M. Passoni, A. Kleyn, P. Zeijlmans van Emmichoven, Deuterium retention and surface modifications of nanocrystalline tungsten films exposed to high-flux plasma, J.Nucl.Mater. 463 (2015) 989–992, https://doi.org/10.1016/j.jnucmat.2014.11.025.

[15] E. Besozzi, et al., Nanosecond laser pulses for mimicking thermal effects on nanostructured tungsten-based materials, Nucl.Fusion 58 (3) (2018), pp. 036 019, https://doi.org/10.1088/1741-4326/aaa5d5.

[16] M. Sala, A. Uccello, D. Dellasega, M. Pedroni, E. Vassallo, M. Passoni, Exposures of bulk w and nanostructured w coatings to medium flux d plasmas, Nucl.Mater. Energy 24 (2020) 100–779, https://doi.org/10.1016/j.nme.2020.100779.

[17] A. Uccello, et al., Effects of a nitrogen seeded plasma on nanostructured tungsten films having fusion-relevant features, Nuclear Materials and Energy 25 (2020) p. 100 808, https://doi.org/10.1016/j.nme.2020.100808.

[18] J. Yu, W. Han, Z. Chen, K. Zhu, Blistering of tungsten films deposited by magnetron sputtering after helium irradiation, Fusion Eng. Des. 129 (2018) 230–235, https://doi.org/10.1016/j.fusengdes.2018.02.091, issn: 0920-3796.

[19] M. Siccinio, et al., Demo physics challenges beyond iter, Fusion Eng.Des. 156 (2020) 111–603, https://doi.org/10.1016/j.fusengdes.2020.111603.

[20] M.R. Gilbert, S. Zheng, R. Kemp, L.W. Packer, S.L. Dudarev, J.-C. Sublet, Comparative assessment of material performance in demo fusion reactors, Fusion Sci.Technol. 66 (1) (2014) 9–17, https://doi.org/10.13182/FST13-751.

[21] T.W. Morgan, P. Rindt, G.G. van Eden, V. Kvon, M.A. Jaworksi, N.J.L. Cardozo, Liquid metals as a divertor plasma-facing material explored using the pilot-PSI and magnum- PSI linear devices, Plasma Phys.Controlled Fusion 60 (1) (2017) 014–025, https://doi.org/10.1088/1361-6587/aa86cd.

[22] S. Roccella, G. Dose, R. de Luca, M. Iafrati, A. Mancini, G. Mazzitelli, Cps based liquid metal divertor target for eu-demo, J. Fusion Energ. 39 (6) (2020) 462–468, https://doi.org/10.1007/s10894-020-00263-4.

[23] A. Vertkov, I. Lyublinski, M. Zharkov, G. Mazzitelli, M. Apicella, M. Iafrati, Liquid tin limiter for ftu tokamak, Fusion Eng.Des. 117 (2017) 130–134.

[24] N. Kawano, Y. Tamai, M. Kondo, Excellent corrosion resistance of tungsten materials in liquid tin, Plasma Fusion Res. 15 (2020), pp. 1 205 068–1 205 068.

[25] M.J. O'Keefe, J.T. Grant, Phase transformation of sputter deposited tungsten thin films with a-15 structure, J. Appl. Phys. 79 (12) (1996) 9134–9141, https://doi.org/10.1063/1.362584.

[26] A. Lita, et al., Tuning of tungsten thin film superconducting transition temperature for fabrication of photon number resolving detectors, IEEE Trans. Appl. Supercond. 15 (2) (2005) 3528–3531, https://doi.org/10.1109/TASC.2005.849033.

[27] K. Salamon, O. Milat, N. Radić, P. Dubček, M. Jerčinović, S. Bernstorff, Structure and morphology of magnetron sputtered w films studied by X-ray methods, J.Phys. DAppl.Phys. 46 (9) (2013) 095–304, https://doi.org/10.1088/0022-3727/46/9/095304.

[28] T.J. Vink, W. Walrave, J.L.C. Daams, A.G. Dirks, M.A.J. Somers, K.J.A. van den Aker, Stress, strain, and microstructure in thin tungsten films deposited by dc magnetron sputtering, J. Appl. Phys. 74 (2) (1993) 988–995, https://doi.org/10.1063/1.354842.

[29] N. Gordillo, et al., Morphological and microstructural characterization of nanostructured pure -phase w coatings on a wide thickness range, Appl. Surf. Sci. 316 (2014) 1–8, https://doi.org/10.1016/j.apsusc.2014.07.061.

[30] F. Vullers, R. Spolenak, Alpha- vs. beta-w nanocrystalline thin films: a comprehensive study of sputter parameters and resulting materials' properties, Thin Solid Films 577 (2015) 26–34, https://doi.org/10.1016/j.tsf.2015.01.030.

[31] J.T. Gudmundsson, N. Brenning, D. Lundin, U. Helmersson, High power impulse magnetron sputtering discharge, J. Vac. Sci. Technol. A 30 (3) (2012) 030–801, https://doi.org/10.1116/1.3691832.

[32] J.T. Gudmundsson, Physics and technology of magnetron sputtering discharges, p. 113 001, Plasma Sources Sci.Technol. 29 (11) (2020), https://doi.org/10.1088/1361-6595/abb7bd.

[33] A. Anders, J. Andersson, A. Ehiasarian, High power impulse magnetron sputtering: current-voltage-time characteristics indicate the onset of sustained self-sputtering, J. Appl. Phys. 102 (11) (2007) 113–303, https://doi.org/10.1063/1.2817812.

[34] N. Brenning, J.T. Gudmundsson, M.A. Raadu, T.J. Petty, T. Minea, D. Lundin, A unified treatment of self-sputtering, process gas recycling, and runaway for high power impulse sputtering magnetrons, Plasma Sources Sci. Technol. 26 (12) (2017), https://doi.org/10.1088/1361-6595/aa959b, pp. 125 003.

[35] D. Lundin, J. Gudmundsson, T. Minea, High Power Impulse Magnetron Sputtering: Fundamentals, Technologies, Challenges And Applications, Elsevier, 2020, https://doi.org/10.1016/C2016-0-02463-4 isbn: 9780128124543.

[36] I.-L. Velicu, et al., Enhanced properties of tungsten thin films deposited with a novel hipims approach, Appl. Surf. Sci. 424 (2017) 397–406, https://doi.org/10.1016/j.apsusc.2017.01.067, issn: 0040- 6090.

[37] A. Engwall, S. Shin, J. Bae, Y. Wang, Enhanced properties of tungsten films by high- power impulse magnetron sputtering, Surf. Coat. Technol. 363 (2019) 191–197, https://doi.org/10.1016/j.surfcoat.2019.02.055, issn: 0257-8972.

[38] T. Shimizu, et al., Low temperature growth of stress-free single phase -w films using hip- ims with synchronized pulsed substrate bias, J. Appl. Phys. 129 (15) (2021) 155–305, https://doi.org/10.1063/5.0042608.

[39] J.T. Gudmundsson, Ionization mechanism in the high power impulse magnetron sputtering hipims discharge, J. Phys. Conf. Ser. 100 (8) (2008), https://doi.org/10.1088/1742-6596/100/8/082013, pp. 082 013.

[40] M.A. Raadu, I. Axnäs, J.T. Gudmundsson, C. Huo, N. Brenning, An ionization region model for high-power impulse magnetron sputtering discharges, Plasma Sources Sci.Technol. 20 (6) (2011), https://doi.org/10.1088/0963-0252/20/6/065007, pp. 065 007.

[41] H. Eliasson, et al., Modeling of high power impulse magnetron sputtering discharges with graphite target, Plasma Sources Sci. Technol. 30 (11) (2021), https://doi.org/10.1088/1361-6595/ac352c, pp. 115 017.

[42] M. Rudolph, et al., Optimizing the deposition rate and ionized flux fraction by tuning the pulse length in high power impulse magnetron sputtering, Plasma Sources Sci. Technol. 29 (5) (2020) 05LT01, https://doi.org/10.1088/1361-6595/ab8175.

[43] M. Rudolph, et al., Influence of the magnetic field on the discharge physics of a high power impulse magnetron sputtering discharge, J. Phys. D. Appl. Phys. 55 (1) (2022) 015–202, https://doi.org/10.1088/1361-6463/ac2968.

[44] C. Huo, D. Lundin, J.T. Gudmundsson, M.A. Raadu, J.W. Bradley, N. Brenning, Particle-balance models for pulsed sputtering magnetrons, J. Phys. D. Appl. Phys. 50 (35) (2017), https://doi.org/10.1088/1361-6463/aa7d35, pp. 354 003.

[45] J. Gudmundsson, J. Fischer, B. Hinriksson, M. Rudolph, D. Lundin, Ionization region model of high power impulse magnetron sputtering of copper, Surf. Coat. Technol. (2022) 128–189, https://doi.org/10.1016/j.surfcoat.2022.128189, issn: 0257-8972.

[46] N. Brenning, et al., Optimization of hipims discharges: the selection of pulse power, pulse length, gas pressure, and magnetic field strength, J. Vac. Sci. Technol. A 38 (3) (2020), https://doi.org/10.1116/6.0000079, pp. 033 008.

[47] S.S. Babu, et al., Modeling of high power impulse magnetron sputtering discharges with tungsten target, Plasma Sources Sci. Technol. 31 (6) (2022), https://doi.org/10.1088/1361-6595/ac774a, pp. 065 009.

[48] J.W. Bradley, A. Mishra, P.J. Kelly, The effect of changing the magnetic field strength on HiPIMS deposition rates, J. Phys. D. Appl. Phys. 48 (21) (2015), https://doi.org/10.1088/0022-3727/48/21/215202, pp. 215 202.

[49] H. Hajihoseini, et al., The effect of magnetic field strength and geometry on the deposition rate and ionized flux fraction in the hipims discharge, Plasma 2 (2019) 201–221, https://doi.org/10.3390/plasma2020015.

[50] J. Alami, V. Stranak, A. Herrendorf, Z. Hubicka, R. Hippler, Design of magnetic field configuration for controlled discharge properties in highly ionized plasma, Plasma Sources Sci. Technol. 24 (4) (2015), https://doi.org/10.1088/0963-0252/24/4/045016, pp. 045 016.

[51] M. Rudolph, et al., Operating modes and target erosion in high power impulse magnetron sputtering, J. Vac. Sci. Technol. A 40 (4) (2022), https://doi.org/10.1116/6.0001919, pp. 043 005.

[52] B.C. Zheng, D. Meng, H.L. Che, M.K. Lei, On the pressure effect in energetic deposition of Cu thin films by modulated pulsed power magnetron sputtering: a global plasma model and experiments, J. Appl. Phys. 117 (20) (2015) 203–302, https://doi.org/10.1063/1.4921443.

[53] F. Blanco, F.Ferreira da Silva, P. Limão-Vieira, G. García, Electron scattering cross section data for tungsten and beryllium atoms from 0.1 to 5000 eV, Plasma Sources

Sci. Technol. 26 (8) (2017), 085004, https://doi.org/10.1088/1361-6595/aa7b02 issn: 0040-6090.
[54] J. Rezek, T. Kozák, N. Kumar, S. Haviar, Synergy of experiment and model for reactive HiPIMS: effect of discharge parameters on WOsubx/sub composition and deposition rate, J. Phys. D Appl. Phys. 54 (12) (2021) 125–202, https://doi.org/10.1088/1361-6463/abd1a3.
[55] L. Vainshtein, I. Beigman, P. Mertens, S. Brezinsek, A. Pospieszczyk, D. Borodin, Ionization of w atoms and w+ ions by electrons, J. Phys. B Atomic Mol. Phys. 44 (2011) 125–201, https://doi.org/10.1088/0953-4075/44/12/125201.
[56] L.A. Riseberg, W.F. Parks, L.D. Schearer, Penning ionization of Zn and Cd by noble-gas metastable atoms, Phys. Rev. A 8 (4) (1973) 1962–1968, https://doi.org/10.1103/PhysRevA.8.1962.
[57] I. Korolov, G. Bánó, Z. Donkó, A. Derzsi, P. Hartmann, Experimental study of the asymmetric charge transfer reaction between Ar+ ions and Fe atoms, J.Chem.Phys. 134 (6) (2011) 064–308, https://doi.org/10.1063/1.3548657.
[58] J.T. Gudmundsson, D. Lundin, N. Brenning, M.A. Raadu, C. Huo, T.M. Minea, An ionization region model of the reactive ar/osub2/subhigh power impulse magnetron sputtering discharge, Plasma Sources Sci. Technol. 25 (6) (2016), https://doi.org/10.1088/0963-0252/25/6/065004, pp. 065 004.
[59] M. Stenke, et al., Electron-impact single-ionization of singly and multiply charged tungsten ions, J. Phys. B Atomic Mol. Phys. 28 (13) (1995) 2711–2721, https://doi.org/10.1088/0953-4075/28/13/021.
[60] S. Inaba, T. Goto, S. Hattori, Determination of the penning excitation cross sections of Mg atoms by He, Ne and Ar metastable atoms, J. Phys. Soc. Jpn. 52 (4) (1983) 1164–1167, https://doi.org/10.1143/JPSJ.52.1164.
[61] A. Bogaerts, R. Gijbels, Modeling of metastable argon atoms in a direct current glow discharge, Phys. Rev. A 52 (1995) 3743–3751, https://doi.org/10.1103/PhysRevA.52.3743.
[62] A. Bogaerts, R. Gijbels, R.J. Carman, Collisional–radiative model for the sputtered copper atoms and ions in a direct current argon glow discharge, Spectrochim. Acta B At. Spectrosc. 53 (12) (1998) 1679–1703, https://doi.org/10.1016/S0584-8547(98)00201-8, issn: 0584-8547.
[63] A. Bogaerts, R. Gijbels, Relative sensitivity factors in glow discharge mass spectrometry: the role of charge transfer ionization, J. Anal. At. Spectrom. 11 (9) (1996) 841–847, https://doi.org/10.1039/JA9961100841.
[64] A. Bogaerts, K.A. Temelkov, N.K. Vuchkov, R. Gijbels, Calculation of rate constants for asymmetric charge transfer, and their effect on relative sensitivity factors in glow discharge mass spectrometry, Spectrochim. Acta B At. Spectrosc. 62 (4) (2007) 325–336, https://doi.org/10.1016/j.sab.2007.03.010, isbn: 9780128124543.
[65] A. Anders, Deposition rates of high power impulse magnetron sputtering: physics and economics, J. Vac. Sci. Technol. A 28 (4) (2010) 783–790, https://doi.org/10.1116/1.3299267.
[66] A.V. Phelps, Z.L. Petrovic, Cold-cathode discharges and breakdown in argon: surface and gas phase production of secondary electrons, Plasma Sources Sci. Technol. 8 (3) (1999) R21–R44, https://doi.org/10.1088/0963-0252/8/3/201.
[67] X. Tang, A.E. Kuehster, B.A. DeBoer, A.D. Preston, K. Ma, Enhanced thermionic emission of mayenite electride composites in an Ar glow discharge plasma, Ceram. Int. 47 (12) (2021) 16 614–16 631, https://doi.org/10.1016/j.ceramint.2021.02.233, issn: 0272-8842.
[68] R. Buschhaus, M. Prenzel, A. von Keudell, Ion-induced secondary electron emission of oxidized nickel and copper studied in beam experiments, no. 2 31, 2022, https://doi.org/10.1088/1361-6595/ac4c4c, p. 025 017.
[69] Guy Buyle, Diederik Depla, Karin Eufinger, Roger De Gryse, Calculation of the effective gas interaction probabilities of the secondary electrons in a dc magnetron discharge, J. Phys. D. Appl. Phys. 37 (12) (2004) 1639–1647, issn: 0022-3727.
[70] C. Huo, Y. Ji, S. Xie, R. Song, Q. Chen, Simulation results of the gas rarefaction and target ion evolution in a chopped high power impulse magnetron sputtering discharge, AIP Adv. 11 (12) (2021) 125–220, https://doi.org/10.1063/5.0062990.
[71] D. Dellasega, F. Mirani, D. Vavassori, C. Conti, M. Passoni, Role of energetic ions in the growth of fcc and crystalline phases in Ti films deposited by hipims, Appl. Surf. Sci. 556 (2021) 149–678, https://doi.org/10.1016/j.apsusc.2021.149678, issn: 0169-4332.
[72] G.G. Stoney, The tension of metallic films deposited by electrolysis, Proc. Roy. Soc. London Ser. A 82 (553) (1909) 172–175, https://doi.org/10.1098/rspa.1909.0021.
[73] C. Huo, D. Lundin, M.A. Raadu, A. Anders, J.T. Gudmundsson, N. Brenning, On the road to self-sputtering in high power impulse magnetron sputtering: particle balance and discharge characteristics, Plasma Sources Sci. Technol. 23 (2) (2014), https://doi.org/10.1088/0963-0252/23/2/025017, pp. 025 017.
[74] A. Butler, N. Brenning, M.A. Raadu, J.T. Gudmundsson, T. Minea, D. Lundin, On three different ways to quantify the degree of ionization in sputtering magnetrons, Plasma Sources Sci.Technol. 27 (10) (2018), https://doi.org/10.1088/1361-6595/aae05b, pp. 105 005.
[75] K.-H. Lee, J.-K. Yoon, J.-K. Lee, J.-M. Doh, K.-T. Hong, W.-Y. Yoon, Growth kinetics of w5si3 layer in wsi2/w system, Surf. Coat. Technol. 187 (2) (2004) 146–153, https://doi.org/10.1016/j.surfcoat.2004.02.039, issn: 0257-8972.
[76] J. Singh, T. Karabacak, T.-M. Lu, G.-C. Wang, Nanoridge domains in -phase w films, Surf. Sci. 538 (3) (2003) L483–L487, https://doi.org/10.1016/S0039-6028(03)00728-3, issn: 0039-6028.
[77] J. Čapek, M. Hála, O. Zabeida, J.E. Klemberg-Sapieha, L. Martinu, Steady state discharge optimization in high-power impulse magnetron sputtering through the control of the magnetic field, J.Appl.Phys. 111 (2) (2012) 023–301, https://doi.org/10.1063/1.3673871.
[78] G. Abadias, et al., Review article: stress in thin films and coatings: current status, challenges, and prospects, J. Vac. Sci. Technol. A 36 (2) (2018) 020–801, https://doi.org/10.1116/1.5011790.
[79] D. Magnfält, G. Abadias, K. Sarakinos, Atom insertion into grain boundaries and stress generation in physically vapor deposited films, Appl. Phys. Lett. 103 (5) (2013) 051–910, https://doi.org/10.1063/1.4817669.
[80] D. Magnfält, A. Fillon, R.D. Boyd, U. Helmersson, K. Sarakinos, G. Abadias, Compressive intrinsic stress originates in the grain boundaries of dense refractory polycrystalline thin films, J.Appl.Phys. 119 (5) (2016) 055–305, https://doi.org/10.1063/1.4941271.
[81] A. Debelle, G. Abadias, A. Michel, C. Jaouen, V. Pelosin, Growth stress buildup in ion beam sputtered Mo thin films and comparative study of stress relaxation upon thermal annealing or ion irradiation, J. Vac. Sci. Technol. A 25 (5) (2007) 1438–1448, https://doi.org/10.1116/1.2771554.
[82] Can Wang, et al., Effects of oxygen pressure on lattice parameter, orientation, surface mor- phology and deposition rate of (ba0.02sr0.98)tio3 thin films grown on mgo substrate by pulsed laser deposition, Thin Solid Films 485 (1) (2005) 82–89, https://doi.org/10.1016/j.tsf.2005.03.055, issn: 0040-6090.
[83] D. Deniz, T. Karabacak, J.M.E. Harper, Competitive growth mechanisms of aluminum nitride thin films deposited by off-normal reactive magnetron sputtering, J. Appl. Phys. 103 (8) (2008) 083–553, https://doi.org/10.1063/1.2917063.
[84] A. Kossoy, Y. Feldman, R. Korobko, E. Wachtel, I. Lubomirsky, J. Maier, Influence of point-defect reaction kinetics on the lattice parameter of ce0.8gd0.2o1.9, Adv. Funct.Mater. 19 (4) (2009) 634–641, https://doi.org/10.1002/adfm.200801162.
[85] F. Ferreira, J. Oliveira, A. Cavaleiro, Crn thin films deposited by hipims in doms mode, Surf. Coat. Technol. 291 (2016) 365–375, https://doi.org/10.1016/j.surfcoat.2016.02.064, issn: 0257-8972.
[86] A. Anders, A structure zone diagram including plasma-based deposition and ion etching, Thin Solid Films 518 (15) (2010) 4087–4090, https://doi.org/10.1016/j.tsf.2009.10.145, issn: 0040-6090.
[87] J.F. Ziegler, M. Ziegler, J. Biersack, Srim – the stopping and range of ions in matter (2010), Nucl. Instrum. Methods Phys. Res., Sect. B 268 (11) (2010) 1818–1823, https://doi.org/10.1016/j.nimb.2010.02.091, issn: 0168-583X.
[88] M. Rudolph, D. Lundin, E. Foy, M. Debongnie, M.-C. Hugon, T. Minea, Influence of backscattered neutrals on the grain size of magnetron-sputtered tan thin films, Thin Solid Films 658 (2018) 46–53, https://doi.org/10.1016/j.tsf.2018.05.027, issn: 0257-8972.
[89] K. Viskupová, et al., Effect of reflected Ar neutrals on tantalum diboride coatings prepared by direct current magnetron sputtering, no. 9, Surf. Coat. Technol. 421 (2021) 127–463, https://doi.org/10.1016/j.surfcoat.2021.127463.
[90] A. Hakola, et al., Gross and net erosion balance of plasma-facing materials in full-w tokamaks, no. 2, Nucl. Fusion 61 (11) (2021), https://doi.org/10.1088/1741-4326/ac22d2, p. 025 017.
[91] P. Dinca, et al., Negative ion-induced deuterium retention in mixed w-al layers co-deposited in dual-hipims, Surf. Coat. Technol. 363 (2019) 273–281, https://doi.org/10.1016/j.surfcoat.2019.02.019, issn: 0920-3796.
[92] A. Hakola, et al., Ero modelling of net and gross erosion of marker samples exposed to l-mode plasmas on asdex upgrade, Nucl. Mater. Energy 25 (2020) 100–863, https://doi.org/10.1016/j.nme.2020.100863, issn: 2352-1791.
[93] P. McCarthy, D. Hwangbo, M. Bilton, S. Kajita, J.W. Bradley, Enhanced fuzzy tungsten growth in the presence of tungsten deposition, Nucl.Fusion 60 (2) (2020), https://doi.org/10.1088/1741-4326/ab6060, pp. 026 012.
[94] M. Zanáška, et al., Dynamics of bipolar HiPIMS discharges by plasma potential probe measurements, Plasma Sources Sci.Technol. 31 (2) (2022), https://doi.org/10.1088/1361-6595/ac4b65, pp. 025 007.
[95] P. Virtanen, et al., SciPy 1.0: fundamental algorithms for scientific computing in python, Nat. Methods 17 (2020) 261–272, https://doi.org/10.1038/s41592-019-0686-2.
[96] C. Kittel, Introduction to Solid State Physics, Wiley, 2004 isbn: 9780471415268. [Online]. Available: https://books.google.it/books?id=kym4QgAACAAJ.
[97] S. Cui, et al., Characteristics of continuous high power magnetron sputtering (c-hpms) in reactive o2/ar atmospheres, J. Appl. Phys. 129 (24) (2021) 243–301, https://doi.org/10.1063/5.0051296.
[98] C. Geuzaine, J.-F. Remacle, Gmsh: a 3-d finite element mesh generator with built-in pre-and post-processing facilities, Int. J. Numer. Methods Eng. 79 (11) (2009) 1309–1331.
[99] A. Halbach, Sparselizard-the user friendly finite element c++ library, 2017.